



# How Do Magnetic Field Models Affect Astrophysical Limits on Light Axion-like Particles? An X-Ray Case Study with NGC 1275

James H. Matthews<sup>1</sup> , Christopher S. Reynolds<sup>1</sup> , M. C. David Marsh<sup>2</sup> , Júlia Sisk-Reynés<sup>1</sup> , and Payton E. Rodman<sup>1</sup> <sup>1</sup> Institute of Astronomy, University of Cambridge, Madingley Road, Cambridge, CB3 0HA, UK; [matthews@ast.cam.ac.uk](mailto:matthews@ast.cam.ac.uk)<sup>2</sup> The Oskar Klein Centre, Department of Physics, Stockholm University, Stockholm 106 91, Sweden

Received 2022 January 19; revised 2022 February 15; accepted 2022 February 15; published 2022 May 5

## Abstract

Axion-like particles (ALPs) are a well-motivated extension to the standard model of particle physics, and X-ray observations of cluster-hosted AGN currently place the most stringent constraints on the ALP coupling to electromagnetism,  $g_{a\gamma}$ , for very light ALPs ( $m_a \lesssim 10^{-11}$  eV). We revisit limits obtained by Reynolds et al. using Chandra X-ray grating spectroscopy of NGC 1275, the central AGN in the Perseus cluster, examining the impact of the X-ray spectral model and magnetic field model. We also present a new publicly available code, ALPRO, which we use to solve the ALP propagation problem. We discuss evidence for turbulent magnetic fields in Perseus and show that it can be important to resolve the magnetic field structure on scales below the coherence length. We reanalyze the NGC 1275 X-ray spectra using an improved data reduction and baseline spectral model. We find the limits are insensitive to whether a partially covering absorber is used in the fits. At low  $m_a$  ( $m_a \lesssim 10^{-13}$  eV), we find marginally weaker limits on  $g_{a\gamma}$  (by 0.1–0.3 dex) with different magnetic field models, compared to Model B from Reynolds et al. (2020). A Gaussian random field (GRF) model designed to mimic  $\sim 50$  kpc scale coherent structures also results in only slightly weaker limits. We conclude that the existing Model B limits are robust assuming that  $\beta_{\text{pl}} \approx 100$ , and are insensitive to whether cell-based or GRF methods are used. However, astrophysical uncertainties regarding the strength and structure of cluster magnetic fields persist, motivating high-sensitivity RM observations and tighter constraints on the radial profile of  $\beta_{\text{pl}}$ .

*Unified Astronomy Thesaurus concepts:* Particle astrophysics (96); Dark matter (353); X-ray active galactic nuclei (2035); Intracluster medium (858); Extragalactic magnetic fields (507)

## 1. Introduction

Probing physics beyond the standard model (SM) of particle physics is a fundamental goal of modern particle and astroparticle physics. One particularly well-motivated SM extension involves axions. The axion is the particle associated with the Peccei-Quinn field (Peccei & Quinn 1977; Weinberg 1978; Wilczek 1978), and was posited to solve the strong CP problem of Quantum Chromodynamics (QCD; Cheng 1988; Kim & Carosi 2010). Including the QCD axion field naturally leads to CP conservation without a fine-tuning problem. The QCD axion has a one-to-one relationship between its mass,  $m_a$ , and coupling to electromagnetism,  $g_{a\gamma}$ , but a more general class of particles known as axion-like particles (ALPs; see reviews by Graham et al. 2015; Irastorza & Redondo 2018) is predicted by effective theories derived from string theory (Svrcek & Witten 2006). ALPs are appealing dark matter candidates (Preskill et al. 1983; Abbott & Sikivie 1983; Dine & Fischler 1983; Arias et al. 2012; Ringwald 2012; Marsh 2016; Chadha-Day et al. 2021) and can modify astrophysical processes (e.g., Raffelt 1996); their significance for fundamental particle physics, astrophysics, and cosmology is therefore clear.

An important characteristic of ALPs is their coupling to radiation with a mass-independent coupling constant, described by the Lagrangian term

$$\mathcal{L}_{\gamma a} = g_{a\gamma} a(\mathbf{E} \cdot \mathbf{B}), \quad (1)$$

where  $a$  is the ALP field,  $\mathbf{E}$  is the electric field, and  $\mathbf{B}$  is the magnetic field. ALPs couple to two photons, meaning that in the presence of an external magnetic field, ALPs and photons can undergo quantum mechanical oscillations. The property of photon–ALP conversion or “mixing” in external magnetic fields can be used to search for ALPs experimentally, and to place limits in  $(m_a, g_{a\gamma})$  parameter space. Experimental ALP searches are reviewed by Graham et al. (2015); approaches include so-called “light shining through wall” experiments (e.g., Ehret et al. 2009; Arias et al. 2010; Ballou et al. 2014) and axion helioscopes such as the CERN Axion Solar Telescope (CAST; CAST Collaboration et al. 2007; Arik et al. 2009) and the proposed International AXion Observatory (IAXO; Irastorza et al. 2011; Armengaud et al. 2014). The presence of *astrophysical* magnetic fields can also be leveraged to search for ALPs. For example, supernova 1987A provides limits on the photon–ALP coupling from the absence of an associated gamma-ray burst (e.g., Brockway et al. 1996; Raffelt 2008; Payez et al. 2015) and ALPs could induce distortions in the Cosmic Microwave Background (Mukherjee et al. 2019, 2020). Currently, one of the best ways of searching for and constraining light ALPs ( $m_a \lesssim 10^{-9}$  eV) involves searching for irregularities in the spectra of active galactic nuclei (AGN) embedded in magnetized clusters; this method, when applied to the gamma-ray and (in particular) X-ray frequency ranges, is our main focus here.

Wouters & Brun (2013) were the first to place constraints on ALPs from X-ray spectroscopy, using Chandra data from Hydra A. Since then, ALP limits have been acquired from

X-ray observations of M87 (Marsh et al. 2017), NGC 3862 (Conlon et al. 2017), and NGC 1275, the central AGN in the Perseus cluster (Berg et al. 2017; Reynolds et al. 2020, hereafter R20). R20 found constraints on very light ALPs ( $m_a \lesssim 10^{-11}$  eV), ruling out  $g_{a\gamma} > 6\text{--}8 \times 10^{-13} \text{ GeV}^{-1}$  at 99.7% confidence. Marginally tighter constraints still are obtained based on an analysis of the cluster-hosted quasar H1821+643 (Sisk-Reynés et al. 2022). Schallmoser et al. (2021) find similar constraints from five AGN located either within or behind clusters such as Coma, using machine-learning techniques as suggested by Day & Krippendorf (2020). Gamma-ray studies offer slightly weaker, although complementary, constraints at higher masses,  $5 \times 10^{-10} \lesssim (m_a/\text{eV}) \lesssim 5 \times 10^{-9}$ , with Ajello et al. (2016) excluding  $g_{a\gamma} > 5 \times 10^{-12} \text{ GeV}^{-1}$  at 95% confidence.

In the X-ray band, AGN are characterized by a power-law spectrum thought to be produced by inverse Compton scattering of accretion disk seed photons. This power-law spectrum is ubiquitous, but other spectral imprints such as a soft X-ray excess, relativistic reflection signatures, and atomic features such as a 6.4 keV iron line are also extremely common. These astrophysical signatures complicate searches for ALPs, since identifying any spectral irregularity relies on a well-characterized continuum source. While the underlying physics of accretion discs and their associated X-ray coronae, winds and absorbers is complex and poorly understood, from a phenomenological perspective, AGN spectra can nevertheless be well-modeled using a suite of detailed spectral models in tools such as XSPEC (Arnaud 1996). Furthermore, in some cases, the power law is virtually featureless and only simple corrections for intervening soft X-ray absorption are needed, such as in the case of NGC 1275 in the Perseus cluster. However, additional complications stem from instrument calibration, photon pileup and the need to separate the cluster and AGN source (R20).

A major systematic uncertainty in modeling ALP signatures from cluster AGN is the magnetic field structure and strength along our line of sight. This topic is the main focus of our work. The intracluster medium (ICM) is magnetized, and is likely to be turbulent (e.g., Carilli & Taylor 2002; Govoni & Feretti 2004; Schekochihin & Cowley 2006; Donnert et al. 2018; Vazza et al. 2018). Generally speaking, observations are consistent with a tangled magnetic field of  $\sim 1\text{--}10 \mu\text{G}$  strength, decreasing with radius, and a Kolmogorov power spectrum. The turbulence requires energy input, which could come from mergers and/or the central AGN. These processes may also create coherent large-scale fields, but evidence for such structures is relatively weak. Empirical constraints on the field strength can come from Faraday rotation, observed pressure profiles, synchrotron radio haloes, and other model-dependent methods. Each of these has strengths and weaknesses. The quantity that matters for ALP conversion is the perpendicular magnetic field component ( $B_\perp$ ) along the line of sight to the continuum source. The Faraday rotation measure (RM) gives us a line-of-sight measure, but it is an integrated quantity and only includes  $B_\parallel$ . The pressure profile does give an indication of the radial profile, but this is often measured within annuli around the source, so it only corresponds to an accurate line-of-sight measure if a reasonable degree of spherical symmetry applies.

This paper is structured as follows. First, in Section 2, we discuss the physics of ALP–photon conversion and introduce

our new Python package, ALPRO. We then review common models for modeling magnetic fields in clusters in ALP searches in Section 3, and explore the astrophysical evidence for magnetic fields in the Perseus cluster in particular. In Section 4, we conduct a sensitivity study, comparing the results from Gaussian random fields and simpler cell-based approaches and assessing the impact of small-scale field structure. In Section 5, we reanalyze the X-ray data from NGC 1275 in the Perseus cluster, and we present updated limits using various magnetic field models and an improved spectral model. In Section 6, we discuss the application of the Fourier formalism to NGC 1275 as well as the implications for other clusters, before concluding in Section 7. Overall, we find that the astrophysical assumptions about the normalization of the magnetic field strength are important and can modify the limits appreciably while still producing acceptable predicted Faraday rotation measures; however, other specific choices—such as between a cell-based or Gaussian random field approach, or how to set the coherence length of the magnetic field—have a relatively small effect on the limits obtained, introducing a systematic uncertainty of  $\sim 0.1$  dex.

## 2. ALP–Photon Interconversion

The contribution to the Lagrangian from ALPs of mass  $m_a$  can be written as

$$\mathcal{L}_a = -\frac{1}{2}\partial_\mu a \partial^\mu a - \frac{1}{2}m_a^2 a^2 + g_{a\gamma} a (\mathbf{E} \cdot \mathbf{B}), \quad (2)$$

where the final term describes the ALP–photon mixing with coupling constant  $g_{a\gamma}$ . We deal with relativistic ALPs, with  $m_a \ll E$  such that the relevant equation of motion (for propagation in the  $z$ -direction) for a beam energy  $E$  is a first-order Schrödinger-like equation, given by

$$\left( i \frac{d}{dz} + E + \mathcal{M}(z) \right) \begin{pmatrix} |\gamma_x\rangle \\ |\gamma_y\rangle \\ |a\rangle \end{pmatrix} = 0, \quad (3)$$

where  $\mathcal{M}$  is the mixing matrix of the form (Raffelt & Stodolsky 1988)

$$\mathcal{M}(z) = \begin{pmatrix} \Delta_{\text{pl}}(z) & 0 & \Delta_x(z) \\ 0 & \Delta_{\text{pl}}(z) & \Delta_y(z) \\ \Delta_x(z) & \Delta_y(z) & \Delta_a \end{pmatrix}. \quad (4)$$

Here, the dispersive diagonal terms are  $\Delta_a = -m_a^2/(2E)$  and  $\Delta_{\text{pl}}(z) = \omega_{\text{pl}}^2/(2E)$ , where  $\omega_{\text{pl}}$  is the usual plasma frequency. We have neglected the Faraday rotation terms, which are negligible at X-ray and gamma-ray energies. The off-diagonal terms are responsible for photon–ALP mixing and are given by

$$\Delta_x = g_{a\gamma} B_x(z)/2, \quad (5)$$

$$\Delta_y = g_{a\gamma} B_y(z)/2. \quad (6)$$

The Schrödinger-like equation must in general be solved numerically, but analytical calculations are possible for certain configurations, and perturbative treatments are also useful (see, e.g., Section 2.1). More mathematical details are given by other authors (e.g., Raffelt & Stodolsky 1988; de Angelis et al. 2011; Marsh et al. 2017; Davies et al. 2021); here, we focus on

discussing just a few key aspects of the ALP–photon conversion process.

It is informative to consider an idealized case, where the beam is in a pure polarization state,  $(|\gamma_x\rangle, |\gamma_y\rangle, |a\rangle) = (1, 0, 0)$ , and travels a distance  $L$  through a uniform magnetic field of strength  $B$  aligned with the  $x$ -axis. In this case, the off-diagonal  $\Delta_y$  terms are zero and the conversion probability can be shown to be

$$P_{\gamma_x \rightarrow a} = \frac{\Theta^2}{1 + \Theta^2} \sin^2(\Delta_{\text{eff}} \sqrt{1 + \Theta^2}), \quad (7)$$

where we have adopted the notation of Marsh et al. (2017) with  $\Theta = 2B_{\perp} E g_{a\gamma} / m_{\text{eff}}^2$  and  $\Delta_{\text{eff}} = m_{\text{eff}}^2 L / (4E)$ , where  $m_{\text{eff}}^2 = m_a^2 - \omega_{\text{pl}}^2$ . Here, we have given the conversion probability for a polarized beam, but in our work we assume that the X-ray emission is initially unpolarized. The degree of polarization of X-ray emission in AGN is not well-constrained observationally—although this may change with the launch of the Imaging X-ray Polarimetry Explorer [IXPE], as shown by, e.g., Ursini et al. (2022)—and the situation is complicated by the possibility of a composite X-ray source in NGC 1275 (Reynolds et al. 2021; see also Section 5). Models of X-ray polarization signatures from AGN predict an (inclination-dependent) degree of polarization of a few percent from an accretion disk corona (Schnittman & Krolik 2010; Beheshti-pour et al. 2017) and  $\sim 10\%$  from a relativistic jet (McNamara et al. 2009). Given the absence of X-ray polarization data and the lack of knowledge about the detailed physics of the X-ray emitting region(s), we take a standard approach and do not assign any initial preferential polarization to the X-ray beam in our calculation. Additionally, we note that ALPs themselves can introduce polarization—an effect that has been studied by Day & Krippendorf (2018), using NGC 1275 as a candidate source—which has exciting prospects for future X-ray missions such as *IXPE*.

Under our assumptions, the actual multiplicative imprint on the spectrum is determined by the survival probability from an unpolarized beam,  $P_{\gamma\gamma}$ . This unpolarized survival probability can be calculated from the pure polarization case using

$$P_{\gamma\gamma} = (1 - P_{\gamma a}) = 1 - \frac{1}{2}(P_{\gamma_x \rightarrow a} + P_{\gamma_y \rightarrow a}), \quad (8)$$

where  $P_{\gamma a}$  is the total, unpolarized conversion probability. In our work, we will always consider the general case where both  $\Delta_x$  and  $\Delta_y$  are nonzero and  $z$ -dependent. In this case,  $P_{\gamma\gamma}$  must be calculated numerically by formulating a transfer matrix to solve Equation (3). The line-of-sight is split into a series of cells and the calculation is carried out in a piecewise fashion in each cell  $j$ , with the output state  $(|\gamma_x\rangle, |\gamma_y\rangle, |a\rangle)$  used as input to the next cell  $j + 1$ .

### 2.1. The Fourier Formalism

Recently, Marsh et al. (2022) outlined a new formalism for treating relativistic ALP–photon conversion. Marsh et al. (2022) showed that, to leading order in  $g_{a\gamma}$ , the conversion probability  $P_{\gamma \rightarrow a}$  (with  $i \in [x, y]$ ) can be related to  $\Delta_i(z)$ , or equivalently, the magnetic field profile along the line of sight  $B_i(z)$ , using Fourier-like transforms. Although this treatment breaks down when the conversion probabilities

exceed  $\sim 5\%$ – $10\%$ , it is an extremely useful framework when considering how different magnetic field treatments affect the conversion probability, so we shall briefly review the main results. In the massive ALP ( $m_a \gg \omega_{\text{pl}}$ ) case and focusing on the  $x$ -component only, the conversion probability can be written as

$$P_{\gamma_x \rightarrow a}(\eta) = \mathcal{F}_s(\Delta_x)^2 + \mathcal{F}_c(\Delta_x)^2, \quad (9)$$

where  $\mathcal{F}_c$  and  $\mathcal{F}_s$  denote the cosine and sine transforms using a conjugate variable  $\eta = m_a^2 / 2E$ , e.g.,  $\mathcal{F}_c(f) = \int_0^\infty f(z) \cos(\eta z) dz$ . By applying the Wiener–Khinchin theorem, the conversion probability can also be expressed in terms of a cosine transform of the autocorrelation function of the line-of-sight magnetic field,  $c_{B_x}$ , as

$$P_{\gamma_x \rightarrow a}(\eta) = \frac{g_{a\gamma}^2}{2} \mathcal{F}_c(c_{B_x}(L)). \quad (10)$$

In the massless case ( $m_a \ll \omega_{\text{pl}}$ ), the same formalism applies if we transform to new variables. Specifically,  $\Delta_x$  is replaced by the function  $G = 2\Delta_x / \omega_{\text{pl}}^2$ , the line-of-sight distance coordinate is replaced by a phase factor proportional to the electron column density,

$$\varphi = \frac{1}{2} \int_0^z dz' \omega_{\text{pl}}^2(z'), \quad (11)$$

and the conjugate Fourier variable is  $\lambda = 1/E$ . With these transformations, the basic principle is similar to the massive ALP case, as the conversion probability can still be expressed as a simple transform of a function of the line-of-sight perpendicular magnetic field. Although the forms above are for a polarized beam, the unpolarized survival probability can always be obtained directly from Equation (8). We will discuss the applicability of this Fourier formalism to grid calculations for X-ray spectral fitting in Section 6.1.

### 2.2. The ALPRO Python Package

We use our new Python package ALPRO (Axion-Like PROPagation; Matthews 2022), v1.0, to solve the Schrödinger-like equation for the propagation of the photon–ALP beam through a magnetic field model. We briefly introduce the code here. ALPRO solves the ALP–photon mixing problem numerically by formulating transfer matrices, following the method outlined by, e.g., de Angelis et al. (2011). The code is written in Python but uses just-in-time (JIT) compilation as part of the NUMBA library (Lam et al. 2015) to speed up the matrix operations. ALPRO is written in a modular fashion and includes routines for setting up various magnetic field models, including random turbulent fields and uniform field models, which will be expanded upon in the future. The code is publicly available at <https://github.com/jhmatthews/alpro>, with documentation hosted on ReadTheDocs. We have tested the results from our code against analytic results as well as numerical results from the code used by Marsh et al. (2017) and the GAMMAALPS code (Meyer et al. 2014, 2021), finding excellent agreement. ALPRO was used for the ALP survival probability curves used by Sisk-Reynés et al. (2022), and the code includes the adaptive treatment of resonances described therein (see their Appendix B). ALPRO also contains an implementation of the Fourier formalism described by Marsh et al. (2022) and briefly outlined in Section 2.1. This functionality allows the user to

take advantage of fast Fourier transform (FFT) techniques to solve the ALP propagation problem in the massive and massless regime, and is accurate for relatively small conversion probabilities with amplitudes of a few percent (see Marsh et al. 2022 and Section 6.1 for more details on the valid regime for this formalism).

### 3. The Magnetic Field in Perseus and Other Clusters

For a given  $m_a$  and  $g_{a\gamma}$ , the quantities that determine the true  $P_{\gamma\gamma}(E)$  are the perpendicular magnetic field along the line of sight to the X-ray point source,  $B_{\perp}(z)$ , and the plasma frequency and therefore electron density along the line of sight,  $n_e(z)$ . Thus, in addition to  $n_e$ , both the strength and structure of the field matter. We now review what is known about magnetic fields in clusters, focusing particularly on the well-studied Perseus cluster, and discuss the models for the magnetic field used in X-ray ALP searches to date. Throughout this section, we will use  $z$  as the radial coordinate for any spherically symmetric density or magnetic field profile, for consistency with the previous section.

#### 3.1. Observational Constraints on Magnetic Field Strength and Structure in the ICM

Estimating the strength and structure of magnetic fields in the ICM is challenging. Constraints come from Faraday rotation measures (RMs), synchrotron-emitting radio haloes and relics, and the thermal pressure profile of the clusters (see reviews by Carilli & Taylor 2002; Govoni & Feretti 2004). We briefly review what is known about ICM magnetic fields from some of these approaches, with a particular focus on cool-core clusters such as Perseus.

Arguably the most direct probes of ICM magnetic fields are Faraday RMs, which provide a measure of the parallel component of the magnetic field,  $B_{\parallel}$ , as defined by

$$\text{RM} = 812 \text{ rad m}^{-2} \int \left( \frac{B_{\parallel}}{\mu\text{G}} \right) \left( \frac{n_e}{\text{cm}^{-3}} \right) dz, \quad (12)$$

where the integral is evaluated along the line of sight. An advantage of an RM measurement is that it probes the same sightline that is traversed by the hypothetical photon-ALP beam; however, it gives no direct measure of  $B_{\perp}$  and one also needs to know the electron density,  $n_e$ . Nonetheless, we still expect this method to give a reasonable handle on the integrated magnetic field along the line of sight, and at the very least it can be used as a check—any field and density model adopted should not produce RMs that are, on average, dramatically in excess of that observed. Faraday RM maps against extended polarized sources can also be produced, which allow the coherence length and power spectrum of the magnetic field to be inferred (e.g., Ensslin & Vogt 2003; Murgia et al. 2004). In general, Faraday RM observations of clusters are consistent with Kolmogorov turbulence, with magnetic field coherence lengths on the order of a few to tens of kpc (Feretti et al. 1995, 1999; Allen et al. 2001; Clarke et al. 2001; Vogt & Enßlin 2005; Enßlin & Vogt 2006; Guidetti et al. 2008; Bonafede et al. 2010; Govoni et al. 2010; Kuchar & Enßlin 2011). The magnetic field strengths inferred are typically  $B \sim 1\mu\text{G}$ , rising to tens of  $\mu\text{G}$  in the inner regions of cool-core clusters such as Hydra and Perseus. In the core of

the Perseus cluster specifically, Taylor et al. (2006) find substantial RMs in the range  $6500\text{--}7500 \text{ rad m}^{-2}$ . The magnitude of these RMs are consistent with being produced by the ICM, but the pc-scale gradient in RMs reported by Taylor et al. (2006) is harder to reconcile with the kpc-scale fields expected in the ICM, and a contribution from compact, dense filaments may be needed.

Energetic constraints on ICM magnetic field strengths can be derived in synchrotron radio haloes and mini-haloes as well as from gamma-ray observations. Synchrotron radio haloes typically provide field estimates of a few  $\mu\text{G}$  under the assumption of minimum energy (e.g., Giovannini et al. 1993; Feretti et al. 1999; Govoni & Feretti 2004; Bonafede et al. 2014; Kale & Parekh 2016), and these field strengths can easily be higher depending on the fractional pressure of nonradiating particles and the filling factor and geometry of the emitting material. Application of the hadronic minimum energy described by Pfrommer & Enßlin (2004) to Perseus gives a (model-dependent) lower limit on the magnetic field of  $4\text{--}9 \mu\text{G}$  in Perseus (Aleksić et al. 2012).

The radial profile of the magnetic field strength can also be estimated by considering the pressure profile of the cluster. In this case, the thermal pressure as a function of radius can be estimated from deprojected X-ray observations under the assumption of spherical symmetry (e.g., Russell et al. 2008), or from the thermal Sunyaev-Zel'dovich effect (e.g., Planck Collaboration et al. 2013). A magnetic field strength can then be calculated by assuming a plasma  $\beta$ , which we denote  $\beta_{\text{pl}}$ , defined (in Gaussian units) as

$$\beta_{\text{pl}} = \frac{P_{\text{th}}}{(B^2/4\pi)}, \quad (13)$$

where  $P_{\text{th}}$  is the thermal pressure. Although the value of  $\beta_{\text{pl}}$  is uncertain, the canonical value is  $\beta_{\text{pl}} \sim 100$  (e.g., Böhringer et al. 2016; Donnert et al. 2018), which can be estimated from comparison of the inferred magnetic pressures from RM studies with the observed thermal pressures.  $\beta_{\text{pl}} \sim 100$  is also expected if the magnetic energy density is in rough equipartition with the kinetic energy, since the velocity fluctuations in clusters and Perseus specifically are observed to be around 10%–20% of the sound speed (e.g., Zhuravleva et al. 2014; Hitomi Collaboration et al. 2018). Further discussion of the value of  $\beta_{\text{pl}}$  in clusters in the context of ALP studies is given by Marsh et al. (2022) and Sisk-Reynés et al. (2022). For a constant  $\beta_{\text{pl}}$ , the sensitivity of the inferred limits on  $g_{a\gamma}$  to the value of  $\beta_{\text{pl}}$  is straightforward. The transformation  $B_{\perp} \rightarrow fB_{\perp}$  and  $g_{a\gamma} \rightarrow g_{a\gamma}/f$ , where  $f$  is a constant, leaves the conversion probability unchanged. Thus, as long as  $\beta_{\text{pl}}$  is uniform in  $z$ , increasing  $\beta_{\text{pl}}$  by a factor  $f^2$  translates into a weaker limit on  $g_{a\gamma}$  by a factor  $f$ . For a  $\beta_{\text{pl}}$  that varies with  $z$ , the effect is more nuanced and depends on the relative importance of different regions of the cluster in determining the ALP signal. An example of how a variable  $\beta_{\text{pl}}$  with radius—scaling as  $\beta_{\text{pl}}(z) \propto \sqrt{z}$ —would affect the magnetic field profile in Perseus is shown in Figure 1; we examine the impact on the limits obtained in Section 5.3.

Finally, it is important to consider the physics of turbulence in clusters from both an observational and theoretical perspective. The Perseus cluster is clearly a dynamic, disturbed environment, with X-ray images showing bubbles, ripples, and variations in surface brightness, particularly in the cluster core

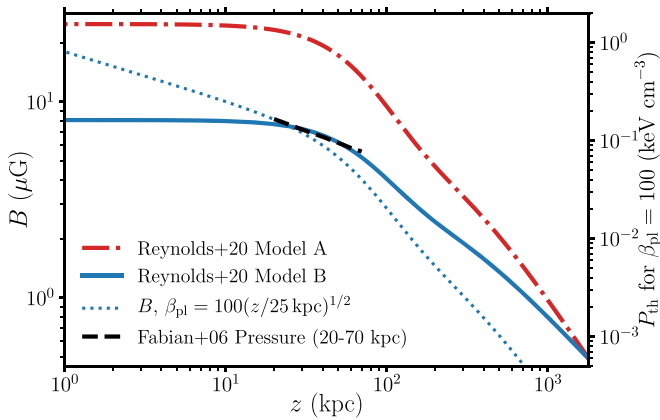


**Figure 1.** Magnetic field strength as a function of radius for Models A and B from R20, compared to the magnetic field inferred from the power-law pressure profile between 20 and 70 kpc from Fabian et al. (2006), assuming  $\beta_{\text{pl}} = 100$ . The dotted line shows the magnetic field strength adjusted from Model B using a variable  $\beta_{\text{pl}}(z) = 100(z/25 \text{ kpc})^{1/2}$ . The right-hand y-axis shows the corresponding thermal pressure for  $\beta_{\text{pl}} = 100$  for Models A and B. By design, Model B matches the thermal pressure at  $\approx 25$  kpc for  $\beta_{\text{pl}} = 100$ , but Model A necessitates a significantly lower value of  $\beta_{\text{pl}}$  in order to avoid overpredicting the thermal pressure at this radius. The variable  $\beta_{\text{pl}}$  model, which only uses the left-hand y-axis, has a slightly stronger field compared to Model B in the inner 10 kpc, but a significantly weaker field on large scales.

(e.g. Fabian et al. 2000; Sanders et al. 2005; Fabian et al. 2006; Sanders & Fabian 2007; Zhuravleva et al. 2014; Walker et al. 2018). The amplitude and power spectrum of velocity fluctuations can be estimated from density fluctuations inferred from observed surface brightness fluctuations (Zhuravleva et al. 2014), giving results that are consistent with Kolmogorov-like turbulence and supporting the emerging picture from ICM Faraday RMs described above. A turbulent ICM is not surprising—while the physics depends on the details of the viscosity, the ICM is thought to have a moderately high effective Reynolds number (Schekochihin et al. 2005; Donnert et al. 2018), meaning that “stirring” of the cluster on large scales will transfer energy to small-scale turbulence via a Kolmogorov-like cascade. The driving scale of the turbulence can be crudely estimated from the Ozmidov scale, the scale on which the turbulent eddy turnover timescale becomes shorter than the buoyancy timescale. Zhuravleva et al. (2014) estimate the Ozmidov scale at  $\sim 10$  s of kpc in the Perseus cluster. Work to understand how the turbulent kinetic energy of the ICM is transferred to magnetic fields is ongoing, but important processes include the small-scale fluctuation dynamos (Schekochihin et al. 2004, 2005), as well as buoyancy and magnetothermal instabilities (Balbus 2000, 2001; Balbus & Reynolds 2010; Perrone & Latter 2021).

Overall, observations imply the presence of  $\sim 10 \mu\text{G}$  strength ICM magnetic fields in cool-core clusters and Perseus specifically. There are also good theoretical and observational reasons to expect the ICM magnetic field to be turbulent on  $\sim \text{kpc}$  scales. We will proceed by using these constraints to design appropriate magnetic field models assuming that a turbulent magnetic field is well-motivated; however, we will also investigate large-scale, “regular” magnetic fields by using a stochastic model that is coherent on  $\gtrsim 50$  kpc scales.

### 3.2. Models Used in Photon-ALP Searches to Date

A common way of parameterizing the magnetic field strength as a function of distance from the cluster center,  $z$ , is

using a power-law function of density such that

$$B(z) = B_0 \left[ \frac{n_e(z)}{n(R_0)} \right]^\alpha, \quad (14)$$

where  $\alpha$  is an exponent typically in the range 0–1 and  $R_0$  is some scaling radius, with  $B_0 \equiv B(R_0)$  providing the normalization of the field. To model  $B(z)$  in Perseus, R20 used two different models for the magnetic field, motivated by previous studies. For Model A, they adopted  $R_0 = 0$ ,  $B_0 = 25 \mu\text{G}$ , and  $\alpha = 0.7$ . Model A is a slightly altered version of the model used by Berg et al. (2017), and is based on very long baseline array (VLBA) observations of NGC 1275. For Model B, they used  $R_0 = 25$  kpc,  $B_0 = 7.5 \mu\text{G}$ , and  $\alpha = 0.5$ . This model is instead based on the radial pressure profile derived by Fabian et al. (2006) from deep X-ray observations (with a total exposure time of 900 ks) of the Perseus cluster, assuming  $\beta_{\text{pl}} = 100$ . We show the magnetic field strength  $B(z)$  for Models A and B of R20 in Figure 1. The thermal pressure profile,  $P_{\text{th}}$ , calculated with  $\beta_{\text{pl}} = 100$ , is plotted on a twin y-axis. We also show the magnetic field strength inferred from the power-law approximation to the thermal pressure between 20 and 70 kpc from Fabian et al. (2006). Model B is based on this pressure profile, so it agrees well with the observed data, but Model A substantially overpredicts the thermal pressure, due to a more optimistic estimate for the magnetic field strength throughout the cluster volume;  $\beta_{\text{pl}} \sim 10$  would be needed to bring agreement with the observed  $P_{\text{th}}$ , which is lower than expected. We therefore adopt the more realistic form of  $B(z)$  from R20 model B for our work (but we also consider a model with variable  $\beta_{\text{pl}}(z)$  in subsequent sections).

It is the perpendicular component of  $\mathbf{B}(z)$  that appears in the ALP mixing matrix (Equations (4)–(6)), so the direction of the field matters, as does its coherence and isotropy. One possible way to model turbulent magnetic fields is using a Gaussian random field (GRF), in which a random, isotropic field is generated according to some power spectrum and then “shaped” so that the field strength decays with radius. GRF models have been used in ALP cluster studies in a number of cases (Wouters & Brun 2012; Angus et al. 2014; Meyer et al. 2014; Schallmoser et al. 2021). Alternatively, a “cell-based” model can be used, in which the magnetic field along the line of sight is modeled as a series of cells of extent  $\Delta z$  (e.g., Wouters & Brun 2012). Each cell is an approximation to a given patch of turbulent field and therefore has a size comparable to the coherence length of the field,  $\Lambda_c$ , a random and isotropic field direction in each cell. The value of  $\Delta z$  is chosen according to a probability distribution function  $p(\Delta z)$ , typically a power law. For example, R20 use  $p(\Delta z) \propto \Delta z^{-1.2}$  spanning 3.5–10 kpc. In their model B, R20 scale these minimum and maximum cell sizes linearly with radius as  $z/50 \text{ kpc}$ , because coherence lengths are expected to grow with distance from the cluster center.

The cell-based method has been used in X-ray studies of M87 (Marsh et al. 2017), NGC 1275 (Reynolds et al. 2020), and H1821+643 (Sisk-Reynés et al. 2022), and is also discussed from a theoretical and modeling perspective by Wouters & Brun (2012), Galanti & Roncadelli (2018), and Marsh et al. (2022). Indeed, Galanti & Roncadelli (2018) suggest that the discontinuities inherent to the cell-based method can introduce unphysical results in the conversion

probability. Cell-based models have continuous magnetic autocorrelation functions consisting of piecewise linear segments, joined at kinks. In the perturbative regime, structure in this autocorrelation function maps directly to structure in the conversion probability that can be interpreted using Fourier analysis (Marsh et al. 2022). Specifically, in this regime, the conversion probability from a cell-based model (and in fact, any discretized model) can be understood as a combination of two effects: (i) an incoherent sum of the oscillatory pattern introduced by each cell and (ii) interference terms whose frequency of oscillation in  $1/E$  is set by the cell boundaries. The jaggedness of the autocorrelation functions of cell-based models leads to enhanced support at high conjugate frequencies, and in the perturbative formalism, this can be understood as excess conversion probability at low energies (Marsh et al. 2022). In many cases of interest, this artificial feature of the cell models only affects the conversion probability below the energy range where it is maximized, and is hence of limited observational importance. For cell models with a constant cell size  $\Delta z$ , unphysical features can be produced with a reciprocal energy spacing that depends on  $\Delta z$ ; in the massive ALP regime, this spacing is  $\Delta(1/E) = 2\pi/(m_a^2 \Delta z)$ , where  $\Delta z$  is in natural (eV) units. However, in practice, a distribution for  $\Delta z$  is often used and  $\Delta z$  is usually fairly small compared to the total path length; both these factors act to wash out and decrease the power in this class of artificial features. Nevertheless, cell-based models are still clearly an approximation to a complex, continuous magnetic field structure.

In addition to  $\mathbf{B}(z)$ , the other important cluster quantity for photon–ALP mixing is the electron density  $n_e$ , which determines the ICM plasma frequency through  $\omega_{\text{pl}} = \sqrt{4\pi n_e e^2 m_e}$ . The density in clusters decreases with radius and is often modeled using a so-called  $\beta$ -law, given by

$$n_e(z) = \left[ 1 - \left( \frac{z}{r_c} \right)^2 \right]^{-3\beta/2}, \quad (15)$$

where  $r_c$  is a core radius and  $\beta$  an exponent of order unity. R20 instead set the density using a double  $\beta$  law, proposed by Churazov et al. (2003) as an analytic approximation to the electron density in the Perseus cluster

$$n_e(z) = \frac{3.9 \times 10^{-2}}{[1 + (z/80 \text{ kpc})^2]^{1.8}} + \frac{4.05 \times 10^{-3}}{[1 + (z/280 \text{ kpc})^2]^{0.87}} \text{ cm}^{-3}. \quad (16)$$

We do expect the electron density to have an impact on the inferred limits on ALP parameters, especially in setting the constraints on  $g_{a\gamma}$  at the high-mass end. However, given that the density is usually well-determined from X-ray observations, we have chosen to focus on the impact of the magnetic field, rather than the density profile, in our work, so we proceed in using Equation (16) for all our photon–ALP conversion calculations hereafter.

#### 4. ALP–Photon Conversion in Turbulent Fields: Model Sensitivity

As discussed above, there are a number of different ways of modeling a turbulent cluster magnetic field, with the cell-based and GRF methods being the most common. We will first

examine the influence of small-scale field structure using a divergence-free GRF, before discussing the ALP survival probability from a mixture of cell-based and GRF models with varying approximations. A turbulent magnetic field can be characterized by its power spectrum, which generally takes a power-law form such that  $E_k dk \propto k^{-n} dk$ , where  $n$  is a power-law index,  $k = 2\pi/\Lambda$  is the wavenumber for a given wavelength  $\Lambda$ , and  $E_k dk$  is the energy contained in the interval  $(k, k + dk)$ . For Kolmogorov turbulence,  $n = 5/3$ . The steeper the index, the more energy is contained (in relative terms) on large scales. It is useful to define the coherence or correlation length of the field, which is the approximate scale upon which the field becomes decorrelated from a neighboring “patch”. For power-law, isotropic turbulence, the coherence length is given by (e.g., Harari et al. 2002)

$$\Lambda_c = \frac{\Lambda_{\text{max}}}{2} \frac{n-1}{n} \frac{1 - (\Lambda_{\text{max}}/\Lambda_{\text{min}})^n}{1 - (\Lambda_{\text{max}}/\Lambda_{\text{min}})^{n-1}}, \quad (17)$$

where  $\Lambda_{\text{min}}$  and  $\Lambda_{\text{max}}$  are the minimum and maximum scale lengths of the turbulence (over which the power spectrum is defined). By considering a few instructive limits, we can see how  $\Lambda_c$  changes for different dynamic ranges and power spectrum indices. In the case of turbulence with a large dynamic range and Kolmogorov index  $n = 5/3$ ,  $\Lambda_c \rightarrow 0.2\Lambda_{\text{max}}$  as  $\Lambda_{\text{max}}/\Lambda_{\text{min}} \rightarrow \infty$ . For very sharply peaked turbulence ( $n \gg 1$  or  $\Lambda_{\text{min}} \rightarrow \Lambda_{\text{max}}$ ),  $\Lambda_c \rightarrow 0.5\Lambda_{\text{max}}$ . Thus, in general, the coherence length can be significantly larger than the smallest scale length. As a result, there can be significant structure and energy contained in modes with  $\Lambda < \Lambda_c$ .

##### 4.1. Generating Random Gaussian Fields

To generate random Gaussian magnetic fields, we follow the approach described by Tribble (1991) and discussed further by various authors (Murgia et al. 2004; Hardcastle 2013; Angus et al. 2014). We first generate random Fourier amplitudes drawn from a Rayleigh distribution, such that the probability density of amplitude  $\mathcal{A}$  is

$$P(\mathcal{A}, \varphi) d\mathcal{A} d\varphi = \frac{\mathcal{A}}{2\pi \mathcal{A}_k^2} \exp\left(-\frac{\mathcal{A}^2}{\mathcal{A}_k^2}\right) d\mathcal{A} d\varphi. \quad (18)$$

where the amplitude is a power law of the form  $\mathcal{A}_k \propto k^{-\zeta}$  defined between minimum and maximum wavenumbers  $k_{\text{min}} = 2\pi/\Lambda_{\text{max}}$  and  $k_{\text{max}} = 2\pi/\Lambda_{\text{min}}$ . The index  $\zeta$  is related to  $n$  by  $\zeta = n + 2$ . We draw phases  $\varphi$  uniformly between 0 and  $2\pi$ . We then take the inverse Fourier transform of the Fourier amplitudes and phases to obtain  $\mathbf{A}$ , the vector potential in real space. We apply the magnetic field radial profile (e.g., from Equation (14)) before calculating the magnetic field as  $\mathbf{B} = \nabla \times \mathbf{A}$ , resulting in a (numerically) divergence-free magnetic field ( $\nabla \cdot \mathbf{B} = 0$ ). We generate a 3D GRF model and then take a single 1D sightline to the center as the input to our photon–ALP conversion calculation. The parameters describing a GRF model are  $\zeta$ , the minimum and maximum scales  $\Lambda_{\text{min}}$  and  $\Lambda_{\text{max}}$ , and the domain size  $z_{\text{max}}$ . For a given field model, the calculation of the ALP survival probability then uses  $N_z$  cells or Fourier samples, which determines the spatial resolution of the model,  $\delta z$ .

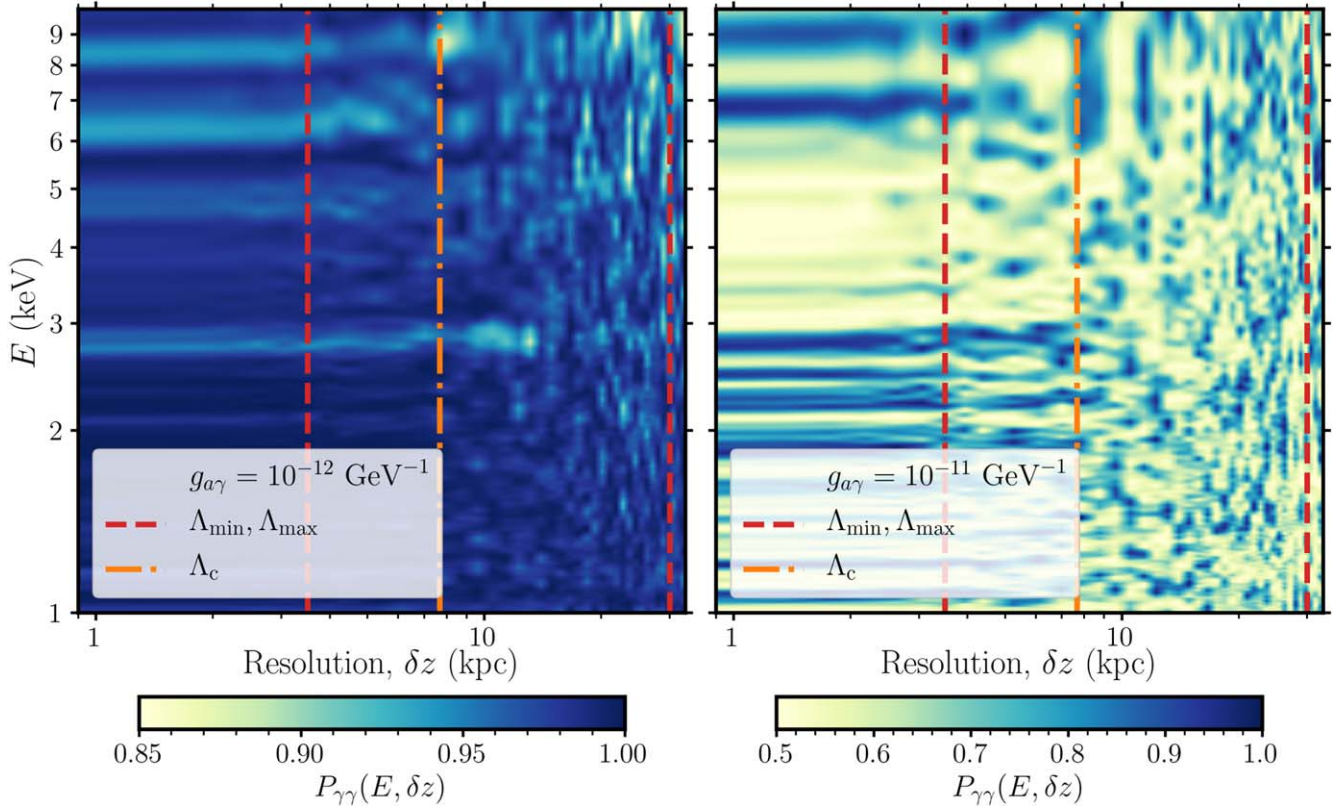


**Figure 2.** The impact of resolution on a single ALP survival curve. The conversion probability is shown as a function of energy  $E$  and resolution  $\delta z$  for a single GRF model realization, for two different values of the coupling constant ( $g_{a\gamma} = 10^{-12} \text{ GeV}^{-1}$ , left, and  $g_{a\gamma} = 10^{-11} \text{ GeV}^{-1}$ , right), and for  $m_a = 10^{-13} \text{ eV}$ . Vertical red dashed lines mark the minimum and maximum scale lengths of the power spectrum ( $\Lambda_{\min}$  and  $\Lambda_{\max}$ ) and the orange dotted-dashed line marks the coherence length  $\Lambda_c$ . The probability stops changing significantly around  $\Lambda_{\min}$ , showing that structure below the coherence length affects the curves and it is important to adequately resolve the field model.

#### 4.2. Sensitivity to Small-scale Field Structure

To examine the sensitivity to small-scale field structure for strong ALP signals, we conducted a resolution test. We first generated 64 different realizations of a GRF model using the procedure described above, with model parameters  $\Lambda_{\min} = 3.5 \text{ kpc}$ ,  $\Lambda_{\max} = 30 \text{ kpc}$ ,  $n = 5/3$ , and  $z_{\max} = 1.8 \text{ Mpc}$ . The profile  $B(z)$  used to shape the magnetic field is that of R20’s Model B, from Equation (14) with  $R_0 = 25 \text{ kpc}$ ,  $\alpha = 0.5$ , and  $B_0 = 7.5 \mu\text{G}$ . Taken together, this choice of parameters corresponds to model 4 as described in Section 4.3, and leads to a coherence length of  $\Lambda_c = 7.67 \text{ kpc}$ . We then calculated survival probability curves in the 1 – 10 keV range at a range of spatial resolutions  $\delta z$ , sampling in the range  $0.25\Lambda_{\min} \leq \delta z \leq 2.5\Lambda_{\min}$  at  $0.25\Lambda_{\min}$  intervals and the range  $2.5\Lambda_{\min} \leq \delta z < 20\Lambda_{\min}$  at  $0.5\Lambda_{\min}$  intervals. We focus on the low-mass ALP case with  $m_a = 10^{-13} \text{ eV}$ , and calculate curves at different coupling constants. We first consider a single field realization and plot the survival probability  $P_{\gamma\gamma}$  as a function of  $\delta z$  and energy  $E$  in Figure 2, for  $g_{a\gamma} = 10^{-12}, 10^{-11} \text{ GeV}^{-1}$ . We do not present results for lower values of  $g_{a\gamma}$ , because they are almost identical to the  $g_{a\gamma} = 10^{-12} \text{ GeV}^{-1}$  case, but with  $P_{\gamma a}$  scaled by a factor of  $g_{a\gamma}^2$ . The survival probability stops changing significantly around  $\Lambda_{\min}$ , showing that structure below the coherence length can be important. It is therefore necessary to resolve the minimum scale length of the magnetic field in these cases, to get an accurate survival probability.

We have checked that this result holds for different field realizations, but to show this explicitly, we can consider the

mean survival probability at each energy marginalized over a random number seed, given by  $\bar{P}_{\gamma\gamma}(E) = [\sum_i P_{\gamma\gamma}(E, i)]/N$ . This quantity is plotted in Figure 3 as a function of energy and color-coded by resolution  $\delta z$  for  $N = 64$ ,  $g_{a\gamma} = 10^{-12} \text{ GeV}^{-1}$  and  $m_a = 10^{-13} \text{ eV}$ . In the bottom panel, we show the (percentage) residual compared to the mean survival probability at the finest resolution ( $\delta z \approx \Lambda_{\min}/4$ ),  $\bar{P}_{\text{fine}}$ , which is assumed to correspond to “ground truth” for this type of field model. Once again, we see that the survival probability converges around  $\Lambda_{\min}$ . Models that are significantly under-resolved can underpredict the survival probability (and thus overpredict the impact of ALPs) by a few percent.

#### 4.3. Comparison of ALP Signals from Five Different Magnetic Field Models

Our aim is to investigate how the photon–ALP survival probabilities, and resulting limits on photon–ALP coupling,  $g_{a\gamma}$ , depend on the magnetic field model used. To this end, we use five different field models:

1. Model 1: A cell-based magnetic field model as Model B in R20.
2. Model 2: As model 1, but without the linear scaling of cell size  $\Delta z$  with radius.
3. Model 3: As model 1, but with a variable  $\beta_{\text{pl}}(z)$  such that  $B(z)$  is scaled by  $[100/\beta_{\text{pl}}(z)]^{1/2}$ . This model is designed to be consistent with the available magnetic field constraints and  $\beta_{\text{pl}} = 100$  in the cluster core, but allows for the  $\beta_{\text{pl}}(z)$  to increase with distance from the cluster

**Table 1**  
Magnetic Field Models Used to Calculate Photon–ALP Survival Probabilities (e.g., Figure 5) and to Obtain Limits on ALP Parameters in Figure 8

Model	$N$	$B$ -Field	$\Lambda_c$ Scaling?	$\beta_{\text{pl}}(z)$	Range of Scales (kpc)	$\Lambda_c$ (kpc)	Median $ \text{RM} $ (rad m $^{-2}$ )	Color
1	200	Cell-based	Yes	Constant, 100	3.5–10	...	1915	■
2	200	Cell-based	No	Constant, 100	3.5–10	...	1603	■
3	200	Cell-based	Yes	$100 \sqrt{z}/25$ kpc	3.5–10	...	2045	■
4	200	GRF	No	Constant, 100	3.5–30	7.67	2480	■
5	200	GRF	No	Constant, 100	25.125–225	57.1	5050	■

**Note.** The colors shown in the last column match the colors used in the relevant figures. Each model uses the same radial profile for  $B(z)$  as model B from R20, except for model 3, which adjusts this by a factor  $[100/\beta_{\text{pl}}(z)]^{1/2}$ .

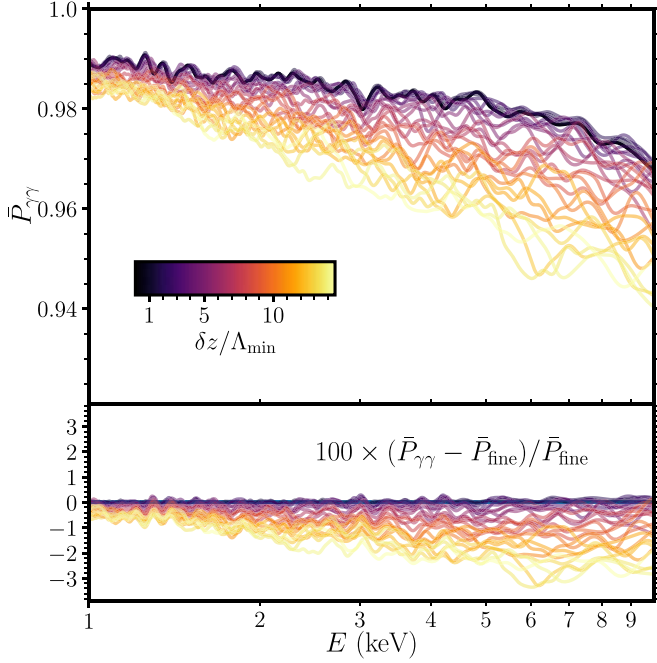


**Figure 3.** Mean survival probability for  $m_a = 10^{-13}$  eV and  $g_{a\gamma} = 10^{-12}$  GeV $^{-1}$ , color-coded by resolution  $\delta z$ , calculated from  $N = 64$  realizations of the GRF model described in Section 4.2 (model 4 in latter sections). The bottom panel shows the percentage residual with respect to  $\bar{P}_{\text{fine}}$ , defined as the mean survival probability of the model at the finest resolution (i.e., the closest to the true survival probability).

center. Such an effect could be produced if, for example, magnetic field amplification is less effective in the outer regions of the cluster. This choice of  $\beta_{\text{pl}}(z)$  is more conservative in terms of the value of  $B_{\perp}$  in the cluster outskirts.

4. Model 4: A Gaussian random field model with Kolmogorov power spectrum and minimum and maximum scale lengths of 3.5 kpc and 30 kpc, respectively.
5. Model 5: A Gaussian random field model with Kolmogorov power spectrum and minimum and maximum scale lengths of 25.125 kpc and 225 kpc, respectively. This model is designed to approximate magnetic fields that are coherent on fairly large scales in the cluster core, but still allows us to marginalize over multiple field realizations.

Parameters and more details on the models are given in Table 1. We adopt a minimum radius of 10 kpc for all our calculations, which is slightly more conservative than R20, and a maximum radius of 1.8 Mpc, the virial radius of the Perseus cluster (see Sisk-Reynés et al. 2022 for a discussion of the

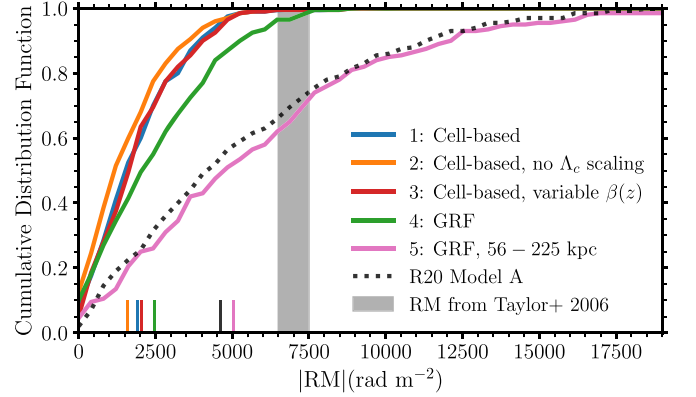


**Figure 4.** Cumulative distribution function of the absolute RMs from 200 realizations of the five magnetic field models used in this work, described in Section 4.3. We also show the RMs from 200 realizations of model A from R20. The median absolute RM for each model is marked with a vertical line on the  $x$ -axis. The shaded region shows the range of RMs reported by Taylor et al. (2006) from observations of the Perseus core (6500–7500 rad m $^{-2}$ ).

sensitivity to these parameters for the H1821+643 limits). The GRF models use a resolution of  $\delta z = \Lambda_{\text{min}}$  informed by the sensitivity study in the previous subsection. Although slightly ad hoc, the choices of scale lengths for models 4 and 5 are made to mimic ICM magnetic fields with qualitatively different structures: model 4 as an approximation to the kpc-scale turbulence typically observed in cool-core clusters, and model 5 to imitate larger-scale coherent modes, which may, for example, be produced by AGN activity. The limitations of these models are discussed further in Section 6.2.

To examine the Faraday RMs predicted by this set of models, we show the cumulative distribution function (CDF) of the absolute value of the RM in Figure 4, compared to the range of values from Taylor et al. (2006). Models 1–4 are quite conservative in their predictions of Faraday RMs, with  $\geq 95\%$  of the realizations producing  $|\text{RM}|$  below the lower bound of the Taylor et al. (2006) measurement (6500 rad m $^{-2}$ ). The median values of  $|\text{RM}|$  for these models lie in the range  $\approx 1500$ –2500 rad m $^{-2}$  (see Table 1 for the exact values). Model 5 predicts slightly higher-magnitude RMs, comparable to model A from R20, which is expected since more coherent fields with significant radial components produce higher RMs (Feretti et al. 1995). However, the median  $|\text{RM}|$  from model 5 is still lower than the observed value, so this field prescription is still broadly consistent with observations. In fact, the expected  $|\text{RM}|$  measurement from models 1 to 5 is below the range inferred by Taylor et al. (2006), implying that our models make fairly reasonable and conservative predictions that are

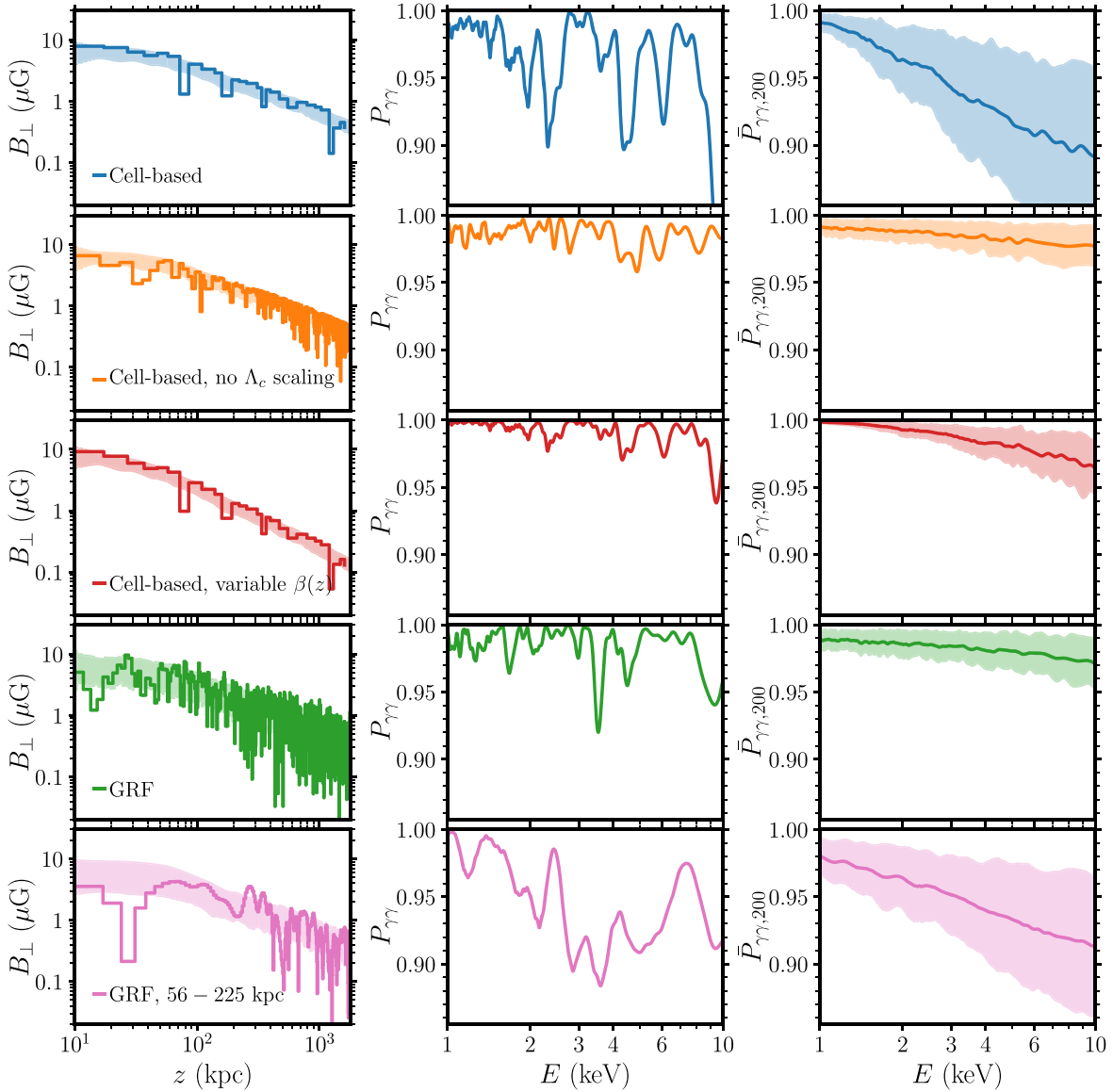


**Figure 5.** The magnetic field models used in this work and their associated photon–ALP survival probabilities. The colors corresponding to each model match those in Table 1 and Figure 8. Left: the profile of the perpendicular magnetic field component,  $B_{\perp}(z)$ , for a single realization of each field model, with the shaded region showing the root-mean-square range of all 200 models. Middle: The survival probability  $P_{\gamma\gamma}$  from the individual field realization as a function of energy in the X-ray band. Right: The mean survival probability averaged over 200 realizations,  $\bar{P}_{\gamma\gamma,200}$ , with the standard deviation of  $P_{\gamma\gamma}$  in each energy bin shown as a shaded region.

generally consistent with observations, albeit somewhat dependent on the exact nature of the Faraday screen.

The line-of-sight profile of  $B_{\perp}(z)$  from a single realization of each of these models is shown in the left-hand panel of Figure 5. The shaded region shows the root-mean-square range of all 200 models. These  $B_{\perp}(z)$  profiles are all stochastically generated using different approaches, so there is no direct equivalence between the realizations, but their general characteristics can still be compared. Some of these characteristics are fairly trivial—for example, we can see that model 3, with the variable  $\beta_{\text{pl}}(z)$ , has a decreased field strength at large radii compared to the fiducial model 1. Similarly, model 2 does not have the scaling factor applied to  $\Delta z$ , resulting in cell sizes that are approximately uniform in linear space, rather than approximately uniform in log-space like models 1 and 3. The cell-based models are clearly qualitatively different from the GRF model with small-scale structure (model 4). First, the cell-based approach does not produce the same small-scale structure

as the GRF model, because it has a minimum cell size of 3.5 kpc and cells are on average significantly larger than this. Second, the dynamic range is smaller because the field strength in each domain is set from Equation (14) with  $R_0 = 25$  kpc,  $B_0 = 7.5 \mu\text{G}$ , and  $\alpha = 0.5$ , and so any variation in  $B_{\perp}(z)$  relative to this results only from the random, isotropic choice of the direction of the vector. In contrast, although  $B_{\perp}(z)$  averages to similar values in the GRF approach, all Fourier modes are accounted for, and in some cases the field is significantly lower or higher than the domains approach, which translates into a larger range in  $B_{\perp}(z)$ ; this effect is discussed by Schallmoser et al. (2021).

#### 4.3.1. Survival Probabilities

For each of our magnetic field models, we use ALPRO to calculate photon survival probabilities  $P_{\gamma\gamma}(E)$  at an energy resolution much finer than the data, using 200 field realizations

(as set by the random number seed) for each of the five magnetic field models. These ALP survival probability curves are used for calculating limits on ALP parameters in the next section, but we can also examine the form of  $P_{\gamma\gamma}(E)$  in each case. The middle panel of Figure 5 shows the survival probability from the same single realization shown in the left-panel, while the right-hand panel shows the mean survival probability calculated from 200 realizations, denoted  $\bar{P}_{\gamma\gamma,200}(E)$ , with the standard deviation shown as a shaded region. There are some notable differences between the characteristics of the curves and the amplitude of the ALP signal. Models 2 and 4 both produce notably larger  $P_{\gamma\gamma}$  and  $\bar{P}_{\gamma\gamma,200}(E)$  (smaller  $P_{\gamma a}$ ), particularly at higher  $E$ , compared to the fiducial cell-based model. Model 3, with the variable  $\beta_{\text{pl}}(z)$ , also produces weaker ALP signals, notably in this case at both low and high  $E$ , due to its decreased magnetic field strength at large radii. The larger-scale GRF model produces features that are quite broad in energy width, as well as an amplitude that is comparable to that of Model 1 and larger than those of Models 2–4.

#### 4.4. Summary of this Section and Literature Comparison

A number of authors have either applied GRF models to ALP cluster studies, considered the drawbacks of cell-based models, or made explicit comparison between GRF and cell-based models (Wouters & Brun 2012, 2013; Angus et al. 2014; Meyer et al. 2014; Galanti & Roncadelli 2018; Schallmoser et al. 2021; Marsh et al. 2022). Wouters & Brun (2012) originally used a cell-based model for their investigation, but they also compared results with those from a Kolmogorov spectrum GRF, finding a broad agreement in the variance of the residuals in their synthetic data. Based on arguments given by Mirizzi et al. (2009); Wouters & Brun (2013) suggest that, in Kolmogorov turbulence, the root-mean-square intensity of the magnetic field varies as  $\Lambda^{1/3}$ , leading to an approximate scaling of the conversion probability as  $P_{\gamma a} \sim \Lambda^{2/3}$ . In this case, we might expect that the small-scale magnetic field would not have a significant impact on photon–ALP conversion. However, the exponent is relatively weak, and will affect small scale lengths that are orders of magnitude below  $\Lambda_c$ . Since  $\Lambda_c \sim \Lambda_{\text{max}}/5$  for broadband Kolmogorov turbulence, scales below the coherence length can still have a significant impact, at the  $\sim 5\%$  level. This approximate scaling is in agreement with our findings and shows that it is important to conduct ALP calculations with a reasonable dynamic range of scales and resolution. This is perhaps an argument against the cell-based models, since these models have no real structure below  $\sim \Lambda_c$ . Having said this, the form of the survival probability from cell-based models and GRF models is actually rather similar, as found in previous studies (Wouters & Brun 2012; Meyer et al. 2014; Schallmoser et al. 2021; Marsh et al. 2022), so while small-scale structure can be important, it is probably a subdominant effect compared to the systematic uncertainty on the radial profiles of  $\beta_{\text{pl}}$  and  $\Lambda_c$ .

Overall, our calculations show that the magnetic field model has an impact on the form of  $P_{\gamma\gamma}(E)$ , which is sensitive to the radial profile and coherence scale of the field. Naïvely, since  $P_{\gamma a} \propto g_{a\gamma}^2$ , we can anticipate that smaller conversion probabilities by a factor of 2 would translate to weaker limits on  $g_{a\gamma}$  by  $\sqrt{2}$ . However, the exact change in the limits is  $m_a$ -dependent and partly dictated by the signal-to-noise in each energy bin, which is a function of the intrinsic source spectrum and the

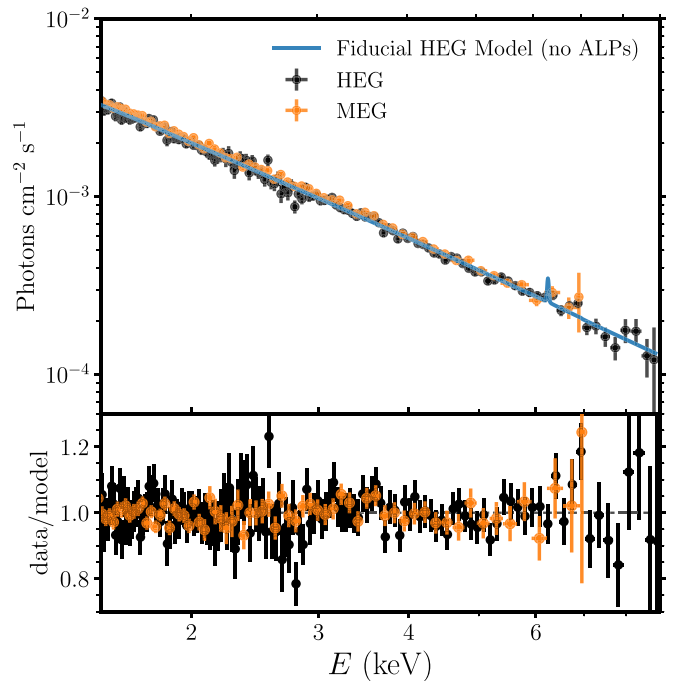


**Figure 6.** Top panel: The best-fitting fiducial model of the form  $\text{tbabs}*\text{tbpcf}(\text{pow}+\text{zgauss})$  to the HEG data (blue) without ALPs, together with the combined HEG (black) and MEG (orange) data from the HETG observations of NGC 1275. The data are shown over the considered HEG energy range (1.5–8.9 keV), although we include MEG data down to 1 keV in our analysis. Bottom: Fit residuals from the best-fit model for each data set. The data have been rebinned for plotting purposes, but all fits are performed on the unbinned data. The MEG best-fit model is identical to the HEG bar minor differences in normalization (see, e.g., Table 2).

observatory/instrument configuration. We therefore conduct a reanalysis of the NGC 1275 Chandra data in the next section using the models described here (but over a wide range of  $m_a$  and  $g_{a\gamma}$ ).

## 5. A Reanalysis of the NGC 1275 X-ray Data

We now turn to observational data, to test the sensitivity of the limits to the effects discussed, using the same five magnetic field models we described in the previous section.

### 5.1. Observational Data and Spectral Modelling

We use the same Chandra High-Energy Transmission Grating (HETG) data as R20 and Reynolds et al. (2021, hereafter R21). Data from the HETG are split into two sets, corresponding to the high-energy grating (HEG) and medium-energy grating (MEG); the spectra are shown in Figure 6. The observations form part of a Cycle-19 Large Project and were taken in 15 separate visits between 2017 October 24 and 2017 December 5, forming a total exposure of 490 ks (see R21 for further details of exposure times and precise dates). The actual reduced data used in this work are from R21, who were able to slightly improve the background subtraction. R21 also describe an improved astrophysical model; they find that using a partially covering absorber not only improves the fit to the data, but also brings the inferred column density closer to the expected value from ALMA observations of the Perseus core (Nagai et al. 2019). Nagai et al. (2019) estimate an  $\text{H}_2$  column density of  $N_{\text{H}_2} \approx 2 \times 10^{22} \text{ cm}^{-2}$  from HCN and HCO+ absorption of the emission from the parsec-scale jet; this line-

**Table 2**  
Parameters Used in the X-ray Spectral Modeling, Given With the Best-fit Values and Error Estimates Obtained from a Spectral Fit without ALPs Present

Free Parameters				
Component	Parameter	Description	HEG	MEG
pow	$A_X$	Power-law Normalization	$8.92_{-0.63}^{+0.67} \times 10^{-3}$	$9.45_{-0.58}^{+0.62} \times 10^{-3}$
pow	$\Gamma_X$	Photon index	$1.92_{-0.04}^{+0.04}$	$1.94_{-0.03}^{+0.03}$
tbpcf	$N_H$ (cm $^{-2}$ )	Column density		$7.54_{-2.38}^{+4.24} \times 10^{22}$
tbpcf	$f_{\text{cov}}$	Covering factor		$9.50_{-4.70}^{+4.53} \times 10^{-2}$
zgauss	$A_{\text{line}}$ (phot cm $^{-2}$ s $^{-1}$ )	Line normalization		$4.06_{-2.29}^{+2.46} \times 10^{-6}$
Frozen Parameters				
Component	Parameter	Description	HEG	MEG
tbabs	$N_H$ (cm $^{-2}$ )	Column Density (Galactic)		$1.32 \times 10^{21}$
Fit statistic (without ALPs)				
	$C/\text{dof}$		4857/4863	

**Note.** Uncertainties quoted are 90% confidence intervals as calculated using the `error` command in XSPEC. All parameter values are quoted at three significant figures with uncertainties given to the same absolute precision. Free parameters spanning both HEG and MEG columns have their values tied.

of-sight H<sub>2</sub> absorbing column is very difficult to reconcile with the observed X-ray power-law, which has a formal 90% confidence limit of  $N_H < 3 \times 10^{19}$  cm $^{-2}$  when fitted with a fully covering cold absorption model (R21). One physical interpretation is that the X-rays come from a composite source: an unabsorbed, compact corona associated with an accretion disk, and a heavily absorbed component associated with a parsec-scale jet, the latter of which contributes  $\approx 15\%$ – $20\%$  of the X-ray continuum. The clumpy molecular gas in the cluster core is clumpy on scales similar to that of the jet (Nagai et al. 2019), so this “partial covering” scenario is reasonable. Following R21, we fit the XSPEC model `tbabs*tbpcf(pow+zgauss)`, which includes partial covering absorption (tbpcf), Galactic absorption (tbabs), and a narrow Gaussian to model the 6.4 keV Fe line (zgauss). For the partial covering absorber, we find a best-fit covering factor of  $f_{\text{cov}} = 9.48(\pm 2.85) \times 10^{-2}$  and a column density  $N_H = 7.63(\pm 2.24) \times 10^{22}$  cm $^{-2}$  when the Galactic column density in the tbabs model is kept fixed at  $1.32 \times 10^{21}$  (Kalberla et al. 2005). If the Galactic column density is allowed to vary, a slightly higher covering factor for the tbpcf model of  $f_{\text{cov}} = 1.75(\pm 0.49) \times 10^{-1}$  is favored, with a Galactic column density of  $1.71(\pm 0.22) \times 10^{21}$ . We keep the Galactic density column fixed in this case, and adopt the best-fit set of parameters given in Table 2 as our baseline astrophysical model for the reanalysis. The best-fit model for the HEG data set is shown in Figure 6, as are the fit residuals (without ALPs) for both the HEG and MEG data.

## 5.2. Statistical Procedure

Our fitting procedure and statistical analysis follows the Bayesian procedure described by (Marsh et al. 2017; see also R20, as well as Section 4 of Sisk-Reynés et al. 2022). We compute a grid of survival probability curves in  $(m_a, g_{a\gamma})$  space with a range of random number seeds  $i$  such that each ALP survival probability curve is defined by three variables  $(m_a, g_{a\gamma}, i)$ . We compute curves in the range  $\log_{10}(m_a/\text{eV}) \in [-13.7, -10.5]$  and  $\log_{10}(g_{a\gamma}/\text{GeV}^{-1}) \in [-13.0, -10.2]$  at 0.1 dex intervals. We follow R20 in assuming that, at lower values of  $g_{a\gamma}$  and  $m_a$ , the ALP curves are statistically indistinguishable from those at the lower limits of our adopted calculation range—an assumption we

have checked—so that results from  $\log_{10}(m_a/\text{eV}) = -13.7$  can be extrapolated down to arbitrarily low  $m_a$ . We consider  $N = 200$  field realizations in each case, which results in a library of 185, 600 survival curves for each of the five magnetic field models we consider. This value of  $N$  is lower than the 500 used by R20, but is necessary in order to prevent prohibitive computational cost given the increased number of field models and the fact that we must generate GRF realizations and consider smaller  $\delta z$  in some cases. Our choice of  $N$  introduces some noise into the limits, but as we shall see, similar results are recovered for comparable assumptions and it is still possible to distinguish systematic differences.

We fit each model to the HEG and MEG spectra by combining the ALPs model with our baseline astrophysical model, such that we fit `tbabs*ALPs(tbpcf*(pow+zgauss))`. For each ALP model, we minimize the Cash (1979) statistic, or  $C$ -statistic, and record the best-fit (lowest) value. We then have a value of  $C(m_a, g_{a\gamma}, i)$  for each model realization, and can construct posterior probabilities of the form

$$\mathcal{P}(m_a, g_{a\gamma}, i) \propto \exp(-C/2), \quad (19)$$

where we assume flat priors in  $\ln m_a$  and  $\ln g_{a\gamma}$  over the range  $\log_{10}(m_a/\text{eV}) \in [-30.0, -11.1]$  and  $\log_{10}(g_{a\gamma}/\text{GeV}^{-1}) \in [-19.0, -10.7]$ . The posterior probabilities are normalized so that

$$\sum_{m_a, g_{a\gamma}, i} \mathcal{P}(m_a, g_{a\gamma}, i) = 1. \quad (20)$$

We then marginalize over the magnetic field realizations  $i$ ,

$$\mathcal{P}(m_a, g_{a\gamma}) = \sum_i^N \mathcal{P}(m_a, g_{a\gamma}, i), \quad (21)$$

to obtain a posterior probability at every point in  $(m_a, g_{a\gamma})$  space, again assuming a flat prior on the field realizations. This marginalization step accounts for the “look-elsewhere effect” due to the unknown magnetic field structure along the line of sight. Limits at a given confidence level can then be calculated by sorting the points in  $\mathcal{P}(m_a, g_{a\gamma})$  and finding the pairs of  $(m_a, g_{a\gamma})$  with the highest  $\mathcal{P}(m_a, g_{a\gamma})$  that cumulatively account for

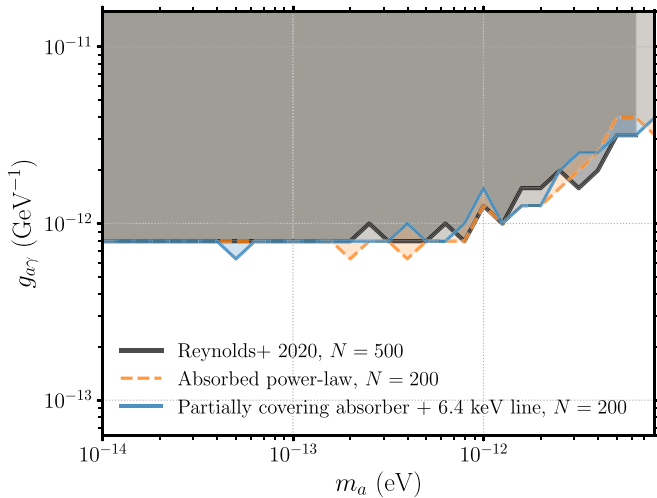


**Figure 7.** The 99.7% limits obtained in this work using two different approaches for modeling the X-ray spectrum, zoomed in to the  $10^{-14} \geq m_a/\text{eV} < 10^{-11}$  region. The partially covering absorber fits use spectral models of the XSPEC form `tbabs*tbpcf(ALPs*(pow+zgauss))`, whereas the absorbed power-law models use `phabs*zphabs(ALPs*pow)`. For comparison, we also show the limits from R20, who used the absorbed power-law method. The limits are not very sensitive to the choice of spectral model, and we reproduce results very similar to those of R20 when using the equivalent spectral model.

the required percentage of the total posterior probability (e.g.,  $\approx 99.7\%$  for a  $3\sigma$  limit). We follow Sisk-Reynés et al. (2022) in grouping pairs with identical  $\mathcal{P}$  and assigning each pair the mean cumulative  $\mathcal{P}$  of the group. This choice has only a very small cosmetic effect on the shape of the inferred limits.

### 5.3. Limits on ALP Parameters

We calculate 99.7% limits on ALP parameters using the above procedure and baseline spectral model, but now including ALPs. We calculated limits with two different spectral models: the partially covering absorber models use models of the XSPEC form `tbabs(ALPs*tbpcf(pow+zgauss))`, whereas the absorbed power-law models use `phabs*(ALPs*zphabs(pow))`. We also model the magnetic field in five different ways, as described in Section 4.3 and summarized in Table 1.

We begin by examining the limits obtained with the two different X-ray spectral models; these limits are shown in Figure 7, zoomed in to the  $m_a \geq 10^{-14}$  eV region, and are also compared to the Model B limits from R20. The first result apparent from Figure 7 is that we obtain limits very similar to those of R20 when using our code ALPRO, acting as an independent test of the R20 results and showing that our new code behaves as expected. Without ALPs, the partially covering absorber plus 6.4 keV emission line model gives  $C/\text{dof} = 4857/4863$ , compared to  $C/\text{dof} = 4923/4865$  for the simple absorbed power-law model. This improvement in goodness of fit might be expected to give slightly tighter limits on  $g_{a\gamma}$ . However, the limits obtained with the improved spectral model are extremely similar to those obtained with the simpler absorbed power-law, with near-identical results at low mass ( $m_a \lesssim 10^{-13}$  eV) and only small differences for  $m_a \gtrsim 10^{-13}$  eV, where the limits are, in any case, slightly noisy. We thus conclude that the limits are insensitive to the details of the approach used to model the X-ray spectrum of

NGC 1275, as long as a physically sensible astrophysical model is used that adequately reproduces the data.

In Figure 8, we show the 99.7% limits obtained with the five different models for the magnetic field, now over a wider range in  $m_a$ . Here, we do see some diversity in the limits obtained. Models 2, 4, and 5 produce slightly weaker limits than R20 at low mass ( $m_a \lesssim 10^{-13}$  eV), by 0.1 dex, ruling out  $g_{a\gamma} > 10^{-12}$  GeV $^{-1}$  at 99.7% confidence. Weaker limits from model 2, which does not scale the coherence length (or more accurately, the cell size  $\Delta z$ ) with radius, would already be expected based on the mean survival probability curves shown in Figure 5. There, the mean survival probability from model 2 is significantly higher than in model 1, due only to the different scalings of  $\Delta z$ , and this translates directly into slightly weaker limits on  $g_{a\gamma}$ . Since model 4 uses a GRF without any scaling of  $\Lambda_c$  with  $z$ , the agreement with the equivalent cell-based model (model 2) shows that the exact choice of how to model the spatial structure of the field (cell-based versus GRF) is a sub-leading effect.

The results from model 5, the “large-scale” GRF model, are particularly interesting. This model is designed to approximate larger scale magnetic field structures in the cluster that are coherent on large scales of  $\gtrsim 50$  kpc. Libanov & Troitsky (2020) have recently suggested that large-scale, coherent, or “regular” field structures in the ICM might significantly weaken ALP limits using a similar method to ours, but applied to gamma-ray observations of NGC 1275. They use a uniform bubble model originally described by Gourgouliatos et al. (2010), with a maximum radius of 93 kpc. In our case, the limits do weaken slightly using the large-scale GRF model, but the effect is small. Our overall conclusion is that, even if coherent large-scale ( $\gtrsim 50$  kpc) magnetic fields are present in Perseus, these do not necessarily significantly weaken the limits on  $g_{a\gamma}$  for low-mass ALPs. Some of these conclusions may be sensitive to the way we decided to model the magnetic field, and the result may be different with alternative data sets; however, we stress that our stochastic model allows us to calculate the limits while still including the “look-elsewhere” effect and marginalizing over random number seed, which was not accounted for in the Libanov & Troitsky (2020) analysis. Although we use a different data set and wave band, our results suggest that the significantly weaker limits found by Libanov & Troitsky (2020) are specific to the field model adopted, rather than being a general feature of large-scale ICM magnetic fields that are coherent over 50–200 kpc.

Model 3, with the variable  $\beta_{\text{pl}}(z)$ , produces the least stringent limits on  $g_{a\gamma}$ , weaker by 0.3 dex at low mass, and is a clear outlier. Inspecting the right-hand panel of Figure 5, this might initially seem surprising, since the conversion probability is comparable in amplitude to models 2 and 4. However,  $\beta_{\text{pl}}$  increases to  $\approx 630$  at 1 Mpc, translating to significantly decreased magnetic fields at large distances and a correspondingly smaller product  $(B_{\perp} L)^2$ . This leads to a small ALP signal at low  $E$  in particular. Since the highest signal-to-noise ratio is obtained at low energies (closer to 1 keV) in both the HEG and MEG data, the limits are particularly sensitive to the conversion probability in this region, explaining the relatively weak limits for this variable  $\beta_{\text{pl}}(z)$  model.

At  $m_a \gtrsim 10^{-12}$  eV, the limits on  $g_{a\gamma}$  span a range of  $\approx 0.5$  dex. Models 2 and 4, neither of which scale  $\Lambda_c$  with radius, actually produce slightly more stringent limits at  $m_a \gtrsim 10^{-12}$  eV than obtained by R20. Conversely, the large-scale GRF model

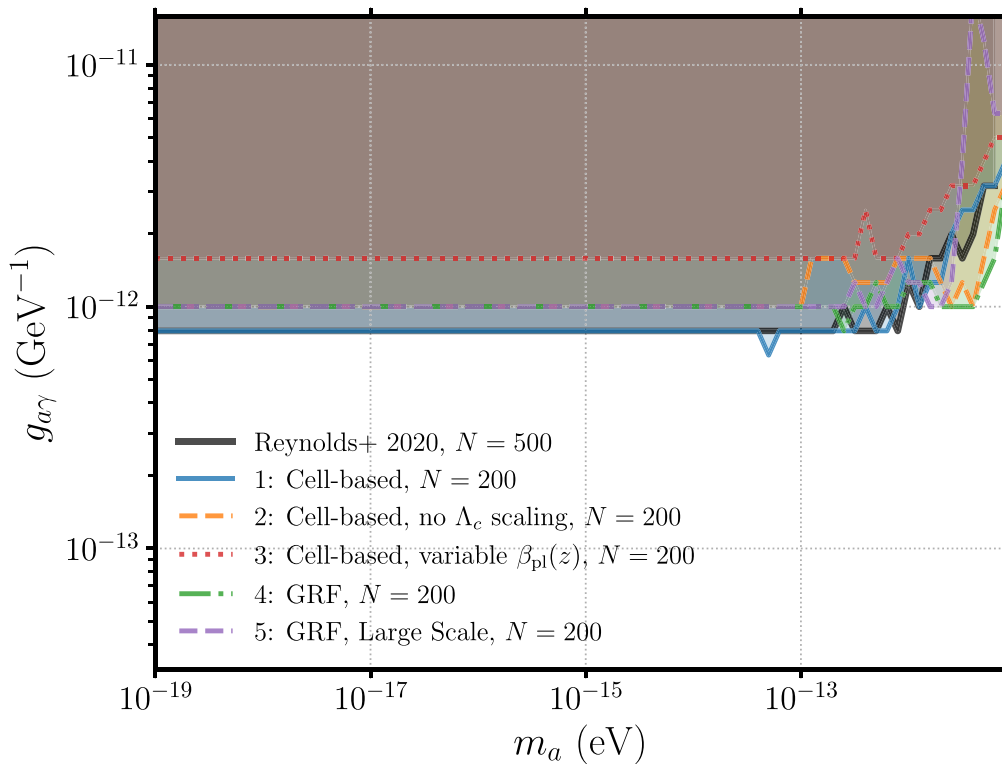


**Figure 8.** How does the choice of magnetic field model affect the NGC 1275 X-ray limits on light axion-like particles? A comparison of 99.7% ALP limits obtained using different approaches for modeling the magnetic field. The models used are given in Table 1, and the colors of the lines match those in the table and in Figure 5. The limits typically vary by 0.1 dex at  $m_a < 10^{-14}$  eV, with the most pessimistic model (model 3) resulting in weaker constraints on  $g_{a\gamma}$  by 0.3 dex. Overall, the limits obtained are not very sensitive to whether a cell-based or GRF approach is used, and the choices made about the coherence length of the magnetic field only change the limits by 0.1 dex.

results in weaker limits in the same mass range. However, this section of the constraints plots is rather noisy in most models, perhaps due to us needing to use  $N=200$  realizations of the magnetic field (rather than, say,  $N=500$  as used by R20). Generally speaking, the shape of the high- $m_a$  envelope of the constraints appears to be quite sensitive to the magnetic field model used, particularly the scale lengths in the magnetic field model. Our results suggest that this region of parameter space—where  $m_a$  is comparable to the range of  $\omega_{pl}$  in the cluster—should be treated with caution when interpreting ALP limits from cluster-hosted AGN.

## 6. Discussion and Applications

### 6.1. Application of the Fourier Formalism

The Fourier formalism developed by Marsh et al. (2022) and described briefly in Section 2.1 can be applied to the problem of photon–ALP conversion in the Perseus cluster. Marsh et al. (2022) already presented results from a model appropriate for Perseus, using a simple single  $\beta$ -law (Equation (15)) for the massless ALP case and neglecting  $n_e$  in the massive ALP case. Here, we repeat similar calculations using discrete cosine transforms (DCTs) across a wide range of parameter space and record the level of agreement with the more general numerical Schrödinger-like equation (NSLE) solution. We consider both the massive and massless regimes, which are determined by the range of  $\omega_{pl}$  in the Perseus cluster. For the purposes of this application, we neglect the “general” case described by Marsh et al. (2022), in which a resonant point (at which  $m_a = \omega_{pl}$ ) is crossed along the path  $z$ .

In the massless case, where  $m_a < \omega_{pl}$ , it is necessary to calculate a phase  $\varphi$ , defined as

$$\varphi(z) = \frac{1}{2} \int_0^z \omega_{pl}(z') dz'. \quad (22)$$

As with a single  $\beta$ -law,  $\varphi$  can be calculated analytically for Equation (16), but we use a numerical Simpson integration for generality. For a single GRF field realization ( $i=0$ ), and for both  $x$  and  $y$  polarization, we compute the function  $G(\varphi) = g_{a\gamma} B_x / \omega_{pl}^2$  and then calculate  $c_G$ , the autocorrelation function of  $G$  in  $\varphi$ -space. We then calculate the conversion probability  $P_{\gamma \rightarrow a}$  by taking the DCT of  $c_G$  with  $N_{\text{det}} = 10^5$  Fourier samples and a conjugate variable  $1/E$ . In the massive case, we essentially repeat the above exercise but without the calculation of  $\varphi$ , instead calculating the autocorrelation function of the magnetic field in real space,  $c_{B_x}$ , and taking the DCT of this to obtain  $P_{\gamma \rightarrow a}$ , with conjugate variable  $\eta = m_a^2 / (2E)$ . Once  $P_{\gamma \rightarrow a}$  and  $P_{\gamma \rightarrow \gamma}$  are known, the unpolarized survival probability  $P_{\gamma\gamma}$  follows from Equation (8). The full procedure in both cases is described in detail by Marsh et al. (2022).

We focus on X-ray energies (1–10 keV) in the massless ALP case. In the massive ALP regime, the energy range depends on  $m_a$  (from the definition of  $\eta$ ). We consider an energy range  $0.1\text{--}100(m_a/10^{-9})^2$  GeV, which is broadly appropriate for the NGC 1275 Fermi-derived limits from Ajello et al. (2016). We evaluate the agreement with the NSLE method by recording the normalized root-mean-square

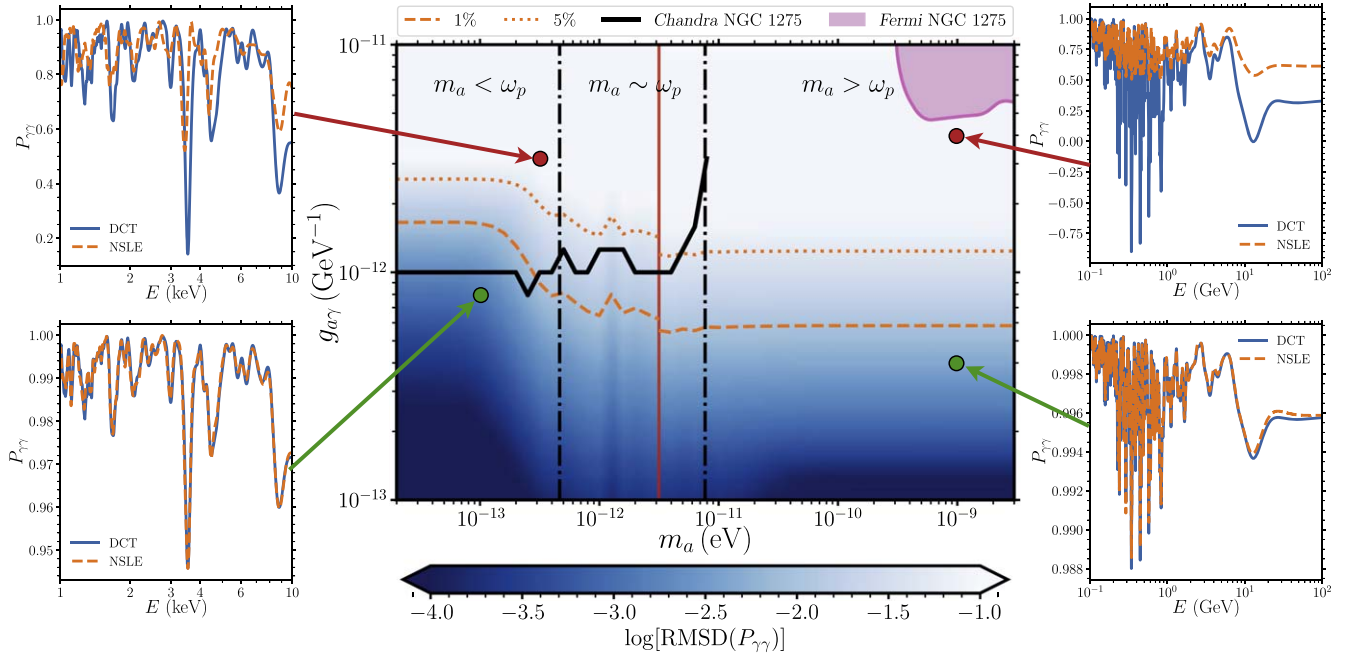


**Figure 9.** A demonstration of the application of the Fourier formalism to the Perseus cluster across a range of  $(m_a, g_{a\gamma})$  parameter space, described in Section 6.1. The color map in the central panel shows the level of agreement between the DCT/Fourier and NSLE approaches, as measured by the logarithm of the root-mean-square deviation (RMSD), from Equation (23). The dashed (dotted) orange line marks the  $\text{RMSD} = 0.01$  ( $\text{RMSD} = 0.05$ ) contour, the vertical dotted–dashed lines mark the range of  $\omega_{\text{pl}}$  in our model for the Perseus cluster, and the vertical red line marks the value of  $m_a$  below (above) which the massless (massive) formalism is used to calculate  $P_{\gamma\gamma}$ . The NGC 1275 ALP limits from Fermi (Ajello et al. 2016) and Chandra (our model 4) are also plotted. We show a comparison of the computed  $P_{\gamma\gamma}$  for four different locations in parameter space spanning both the massless and massive ALP regime. Overall, the figure demonstrates the potential of the Fourier formalism and shows it can already be applied to data with constraining power comparable to those used to obtain X-ray limits from NGC 1275.

deviation, defined as

$$\text{RMSD}(P_{\gamma\gamma}) = \frac{1}{\bar{P}_{\gamma\gamma}^{\text{NSLE}}} \sqrt{\frac{\sum_j^{N_E} (P_{\gamma\gamma}^{\text{NSLE}} - P_{\gamma\gamma}^{\text{DCT}})^2}{N_E}}, \quad (23)$$

where the  $j$  index denotes the energy bin,  $\bar{P}_{\gamma\gamma}$  denotes a mean survival probability averaged over  $N_E$  energy bins, and the NSLE and DCT superscripts refer to the method used to calculate  $P_{\gamma\gamma}$ .

In the central panel of Figure 9, the logarithm of  $\text{RMSD}(P_{\gamma\gamma})$  is plotted as a colormap as a function of  $m_a$  and  $g_{a\gamma}$ , and the 1% and 5% ( $\text{RMSD} = 0.01, 0.05$ ) contours are marked. We compute the survival probability across a wide range of  $m_a$  and  $g_{a\gamma}$ , using the massless formalism for  $\log m_a < -11.5$  and the massive formalism for  $\log m_a > -11.5$ . We show four representative examples of survival probability curves in relevant energy ranges, chosen so that two show good agreement and two do not. The limits from model 4 in this work, and the NGC 1275 Fermi limits from Ajello et al. (2016) are also plotted, and the vertical dotted–dashed lines mark the range of  $\omega_{\text{pl}}$  (at distances 10–1800 kpc from the cluster center) in natural (eV) units, as calculated from Equation (16). If we take the 1% contour of RMSD as constituting reasonable agreement, then the Fourier formalism can already be applied to calculations in the regime of  $g_{a\gamma}$  probed by X-ray observations in the massless ALP regime. In fact, the formalism is likely to give identical statistical results for higher RMSD values comparable to the residuals in the data. The Fermi limits lie at significantly higher  $g_{a\gamma}$ , where the perturbative calculation breaks down, so the Fourier formalism cannot yet be applied to gamma-ray ALP searches. However, the scheme still offers potential for the future if the constraining

power in the GeV regime can be improved by a factor of 10 or so.

By making use of FFT techniques for the DCT, the Fourier formalism can convey a significant performance advantage, but as discussed by Marsh et al. (2022), this speed-up in the calculation depends somewhat on the calculation considered. Using ALPRO, calculating the  $P_{\gamma\gamma}$  curve shown in the bottom right of Figure 9 takes  $\approx 3.9$  s with the NLSE approach with  $N_E = 1000$  energy bins, compared to the Fourier/DCT approach which takes  $\approx 0.7$  s for  $N_{\text{dct}} = 10^5$ . As  $N_E \rightarrow N_{\text{dct}}$ , the speed advantage of the Fourier/DCT approach improves linearly with  $N_E$ , and it can be dramatic. The Fourier formalism is therefore likely to be most useful for high energy resolution or wide energy bands, but even at more modest energy resolutions it already can give extremely fast results for reasonably complex models. The Fourier formalism may also be used to infer information about ALPs and magnetic field structure directly from the residuals in X-ray gamma-ray data. As noted by Marsh et al. (2022), ALP-induced irregularities encode the autocorrelation function of the line-of-sight magnetic field, and it may be possible to map directly from the data residuals to this function (see also Conlon & Rummel 2019; Kachelriess & Tjemsland 2022). The scheme thus offers potential for the future, particularly as a tool for ALP searches with the next-generation *Athena* X-ray telescope (Nandra et al. 2013; Conlon et al. 2018).

## 6.2. Future Work, Limitations, and Implications for Other Clusters

We have chosen to focus on the Perseus cluster in particular, but our results clearly have implications for ALP limits derived from observations of X-ray bright AGN in and behind other

clusters. The limits derived so far in the literature form an inhomogeneous data set with slightly different assumptions in each study. In each case, the availability of RM data and accurate density and pressure profiles varies, while there may be expected to be some intrinsic intercluster variability in, for example, the magnitude of  $\beta_{\text{pl}}$ , or the coherence of the magnetic field. Put simply, we have shown that five magnetic field models that produce similar magnetic pressures in the inner regions of the cluster and a comparable distributions of RMs—both of which are broadly consistent with observations under reasonable assumptions—can produce ALP signals of different strength. One interpretation is that the scatter in the limits in Figure 8 act to crudely encode the systematic uncertainty of the various assumptions in these field models. Based on this reasoning, we might expect that uncertainty on the strength and detailed radial profile of ICM magnetic fields introduces a systematic uncertainty of around 0.3 dex into the various astrophysical limits on ALPs. Moving forward, it would be useful to have a more uniform set of observational constraints on the clusters used for ALP studies to date, through a targeted combination of high-sensitivity RM studies and X-ray observations.

A fruitful avenue for future work would be to use magnetohydrodynamic (MHD) simulations of cluster environments (e.g., Donnert et al. 2009; Xu et al. 2009; Vazza et al. 2014; Beresnyak & Miniati 2016; Vazza et al. 2018) to inform studies such as ours. MHD simulations allow one to study the evolution of magnetic fields in a dynamic environment and the resulting impact on their coherence, strength and overall structure. In addition, magnetic fields may be anisotropic, whereas the GRF model we used assumed isotropy, and ALP signals could be predicted directly from the simulation outputs. Including further insights from MHD simulations, and more generally, gaining a better understanding of the physical processes that govern the magnetized ICM, will be critical for the future of cluster-based ALP studies. One important quantity to constrain—observationally and through MHD modeling—is the value of  $\beta_{\text{pl}}$  in the outer regions of the cluster, since we have shown that the radial profile of  $\beta_{\text{pl}}$  does have an impact on the photon–ALP conversion and resulting limits obtained.

## 7. Conclusions

We have revisited the problem of photon–axion conversion in the Perseus cluster magnetic field with NGC 1275 as a background source. We have reanalyzed the Chandra X-ray data, adopting different approaches to modeling the magnetic field and an improved spectral model. The main result of our work is that, for well-motivated turbulent field models, the limits on  $(m_a, g_{a\gamma})$  obtained by Reynolds et al. (2020) are, in general, quite insensitive to these choices. Overall, the result that  $g_{a\gamma} < 8 \times 10^{-13} \text{ GeV}^{-1}$  for  $m_a < 10^{-12} \text{ eV}$  is robust under the assumption that the ratio of thermal to magnetic pressure in the Perseus cluster is  $\beta_{\text{pl}} \approx 100$ . Our other main conclusions are given below.

1. We review the evidence for turbulent magnetic fields in Perseus. We conclude that turbulent fields are likely, and that Model B of R20 is a reasonable approximation to the magnetic field in Perseus cluster under the justified assumption that  $\beta_{\text{pl}} \approx 100$ . Model A from R20 predicts a pressure profile in excess of that observed for  $\beta_{\text{pl}} = 100$

(equivalently, it predicts a  $\beta_{\text{pl}}$  that is lower than expected in Perseus and other cool-core clusters).

2. We conduct a sensitivity study using a Gaussian random field with the same radial profile as Model B from R20. We examine the sensitivity of the ALP signature to the resolution of the photon–ALP simulations,  $\delta z$ , and discuss this with reference to the scale lengths associated with the turbulence. For a Kolmogorov field, we find that convergence is generally reached at scales below the coherence length, around the minimum scale length of the turbulence, and that under-resolving the magnetic field can lead to overestimates of the ALP signal for a given  $g_{a\gamma}$  and  $\mathbf{B}(z)$ .
3. Informed by the sensitivity study, we reanalyze the NGC 1275 Chandra X-ray data. We use an improved data reduction and X-ray spectral model that accounts for a composite X-ray source surrounded by a clumpy, partially covering absorber. We confirm the basic results from Reynolds et al. (2020), and we find that the limits derived are insensitive to the X-ray spectral model, as long as the spectral models are appropriate and sufficient to describe the data.
4. We rederive limits using the same X-ray data on NGC 1275 for five different magnetic field models. At low  $m_a$  ( $m_a \lesssim 10^{-13} \text{ eV}$ ), marginally weaker limits on  $g_{a\gamma}$  (by 0.1 dex) are obtained with different magnetic field models, including a Gaussian random field model designed to approximate kpc-scale turbulence. Our most pessimistic model, which has a ratio of thermal to magnetic pressure that increases to  $\beta_{\text{pl}} \approx 850$  by the virial radius, predicts weaker limits by 0.3 dex at low  $m_a$ . We conclude that the limits are largely insensitive to whether a cell-based or GRF approach is used to model the magnetic field, or the choices made about the coherence length, but systematic uncertainties relating to the magnitude and radial profile of the magnetic field strength (or, equivalently,  $\beta_{\text{pl}}$ ) persist.
5. Using a “large-scale” GRF model, with magnetic fields that are coherent on  $\gtrsim 50 \text{ kpc}$  scales, only causes the limits at low  $m_a$  to weaken by 0.1 dex. Our work suggests that the significantly weaker limits found by Libanov & Troitsky (2020) are not a general feature of large-scale ICM magnetic fields, and are instead specific to the particular realization of the magnetic field adopted.
6. We show that the new Fourier formalism described by Marsh et al. (2022) can be applied to large regions of the relevant parameter space for a study such as ours, and that they can result in a significant performance improvement when computing photon–ALP survival probability curves.
7. We introduce our new Python package ALPRO for solving the Schrödinger-like equation for ALP–photon propagation. ALPRO also includes an implementation of the Fourier formalism described by Marsh et al. (2022). The code is publicly available at <https://github.com/jhmatthews/alpro>, with accompanying documentation, and is used for all numerical photon–ALP survival probability calculations in this work.

Overall, our work suggests systematic uncertainties in the magnetic field strength and structure along the line of sight remain important to understand. To make progress, further high-sensitivity RM observations across larger regions of the

cluster would be extremely valuable. It is also important to develop a better theoretical and observational understanding of the value of the plasma-beta ( $\beta_{\text{pl}}$ ) in the outer regions of clusters in general. Despite these uncertainties, X-ray observations of cluster-hosted AGN remain one of the most promising and important tools for constraining the properties of very light ALPs.

We thank an anonymous referee for a constructive and helpful report. J.H.M. acknowledges a Herchel Smith Fellowship at Cambridge. C.S.R. thanks the STFC for support under the Consolidated Grant ST/S000623/1, as well as the European Research Council (ERC) for support under the European Union's Horizon 2020 research and innovation program (grant 834203). J.S.R. acknowledges support from the Science and Technology Facilities Council (STFC) under grant ST/V50659X/1 (project reference 2442592). D.M. is supported by the European Research Council under Grant No. 742104 and by the Swedish Research Council (VR) under grants 2018-03641 and 2019-02337. P.E.R. thanks the Gates Cambridge Trust for supporting her doctoral studies. This work was supported, in whole or in part, by the Bill and Melinda Gates Foundation (OPP1144). Under the grant conditions of the Foundation, a Creative Commons Attribution 4.0 Generic License has already been assigned to the Author Accepted Manuscript version that might arise from this submission. The scientific results reported in this article are based in part on observations made by the Chandra X-ray Observatory and published previously in cited articles. This work was performed using resources provided by the Cambridge Service for Data Driven Discovery (CSD3) operated by the University of Cambridge Research Computing Service ([www.csd3.cam.ac.uk](http://www.csd3.cam.ac.uk)), provided by Dell EMC and Intel using Tier-2 funding from the Engineering and Physical Sciences Research Council (capital grant EP/P020259/1), and DiRAC funding from the Science and Technology Facilities Council ([www.dirac.ac.uk](http://www.dirac.ac.uk)). We would like to thank Pierluca Carenza, Jamie Davies, Richard Booth, and Andy Fabian for helpful discussions, and Will Alston for answering some questions about XSPEC. We gratefully acknowledge the use of the following software packages: astropy (Astropy Collaboration et al. 2013, 2018), matplotlib (Hunter 2007), numba (Lam et al. 2015), scipy (Virtanen et al. 2020), pandas (McKinney 2010; Pandas Development Team 2020), OpenMPI (Gabriel et al. 2004) and XSPEC (Arnaud 1996). This paper describes the release of ALPRO v1.0 (Matthews 2022).

### ORCID iDs

James H. Matthews  <https://orcid.org/0000-0002-3493-7737>

Christopher S. Reynolds  <https://orcid.org/0000-0002-1510-4860>

M. C. David Marsh  <https://orcid.org/0000-0001-7271-4115>

Júlia Sisk-Reynés  <https://orcid.org/0000-0003-3814-6796>

Payton E. Rodman  <https://orcid.org/0000-0002-1624-9359>

### References

- Abbott, L.F., & Sikivie, P. 1983, *PhLB*, **120**, 133  
 Ajello, M., Albert, A., Anderson, B., et al. 2016, *PhRvL*, **116**, 161101  
 Aleksić, J., Alvarez, E. A., Antonelli, L. A., et al. 2012, *A&A*, **541**, A99  
 Allen, S. W., Ettori, S., & Fabian, A. C. 2001, *MNRAS*, **324**, 877

- Angus, S., Conlon, J. P., Marsh, M. C. D., Powell, A. J., & Witkowski, L. T. 2014, *JCAP*, **09**, 026  
 Arias, P., Jaeckel, J., Redondo, J., & Ringwald, A. 2010, *PhRvD*, **82**, 115018  
 Arias, P., Cadamuro, D., Goodsell, M., et al. 2012, *JCAP*, **2012**, 013  
 Arik, E., Aune, S., Autiero, D., et al. 2009, *JCAP*, **2009**, 008  
 Armengaud, E., Avignone, F. T., Betz, M., et al. 2014, *JInst*, **9**, T05002  
 Arnaud, K. A. 1996, *ASPC*, **101**, 17  
 Astropy Collaboration, Price-Whelan, A. M., Sipőcz, B. M., et al. 2018, *AJ*, **156**, 123  
 Astropy Collaboration, Robitaille, T. P., Tollerud, E. J., et al. 2013, *A&A*, **558**, A33  
 Balbus, S. A. 2000, *ApJ*, **534**, 420  
 Balbus, S. A. 2001, *ApJ*, **562**, 909  
 Balbus, S. A., & Reynolds, C. S. 2010, *ApJL*, **720**, L97  
 Ballou, R., Deferne, G., Duvillaret, L., et al. 2014, arXiv:1410.2566  
 Beheshtipour, B., Krawczynski, H., & Malzac, J. 2017, *ApJ*, **850**, 14  
 Beresnyak, A., & Miniati, F. 2016, *ApJ*, **817**, 127  
 Berg, M., Conlon, J. P., Day, F., et al. 2017, *ApJ*, **847**, 101  
 Bonafede, A., Feretti, L., Murgia, M., et al. 2010, *A&A*, **513**, A30  
 Bonafede, A., Interna, H. T., Bruggen, M., et al. 2014, *MNRAS*, **444**, L44  
 Brockway, J. W., Carlson, E. D., & Raffelt, G. G. 1996, *PhLB*, **383**, 439  
 Böhringer, H., Chon, G., & Kronberg, P. P. 2016, *A&A*, **596**, A22  
 CAST Collaboration, Andriamionje, S., et al. 2007, *JCAP*, **0704**, 010  
 Carilli, C. L., & Taylor, G. B. 2002, *ARA&A*, **40**, 319  
 Cash, W. 1979, *ApJ*, **228**, 939  
 Chadha-Day, F., Ellis, J., & Marsh, D. J. E. 2021, arXiv:2105.01406  
 Cheng, H. Y. 1988, *PhR*, **158**, 1  
 Churazov, E., Forman, W., Jones, C., & Böhringer, H. 2003, *ApJ*, **590**, 225  
 Clarke, T. E., Kronberg, P. P., & Böhringer, H. 2001, *ApJ*, **547**, L111  
 Conlon, J. P., Day, F., Jennings, N., Krippendorf, S., & Muia, F. 2018, *MNRAS*, **473**, 4932  
 Conlon, J. P., Day, F., Jennings, N., Krippendorf, S., & Rummel, M. 2017, *JCAP*, **2017**, 005  
 Conlon, J. P., & Rummel, M. 2019, *MNRAS*, **484**, 3573  
 Davies, J., Meyer, M., & Cotter, G. 2021, *PhRvD*, **103**, 023008  
 Day, F., & Krippendorf, S. 2018, *Galax*, **6**, 45  
 Day, F., & Krippendorf, S. 2020, *JCAP*, **2020**, 046  
 de Angelis, A., Galanti, G., & Roncadelli, M. 2011, *PhRvD*, **84**, 105030  
 Dine, M., & Fischler, W. 1983, *PhLB*, **120**, 137  
 Donnert, J., Dolag, K., Lesch, H., & Müller, E. 2009, *MNRAS*, **392**, 1008  
 Donnert, J., Vazza, F., Brügggen, M., & Zuhone, J. 2018, *SSRv*, **214**, 122  
 Ehret, K., Frede, M., Ghazaryan, S., et al. 2009, *NIMPA*, **612**, 83  
 Ensslin, T. A., & Vogt, C. 2003, *A&A*, **401**, 835  
 Enßlin, T. A., & Vogt, C. 2006, *A&A*, **453**, 447  
 Fabian, A. C., Sanders, J. S., Ettori, S., et al. 2000, *MNRAS*, **318**, L65  
 Fabian, A. C., Sanders, J. S., Taylor, G. B., et al. 2006, *MNRAS*, **366**, 417  
 Feretti, L., Dallacasa, D., Giovannini, G., & Tagliani, A. 1995, *A&A*, **302**, 680  
 Feretti, L., Dallacasa, D., Govoni, F., et al. 1999, *A&A*, **344**, 472  
 Gabriel, E., Fagg, G. E., Bosilca, G., et al. 2004, in Proc. 11th European PVM/MPI Users' Group Meeting (Berlin: Springer), 97  
 Galanti, G., & Roncadelli, M. 2018, *PhRvD*, **98**, 043018  
 Giovannini, G., Feretti, L., Venturi, T., Kim, K. T., & Kronberg, P. P. 1993, *ApJ*, **406**, 399  
 Gourgouliatos, K. N., Braithwaite, J., & Lyutikov, M. 2010, *MNRAS*, **409**, 1660  
 Govoni, F., Dolag, K., Murgia, M., et al. 2010, *A&A*, **522**, A105  
 Govoni, F., & Feretti, L. 2004, *IJMPD*, **13**, 1549  
 Graham, P. W., Irastorza, I. G., Lamoreaux, S. K., Lindner, A., & van Bibber, K. A. 2015, *ARNPS*, **65**, 485  
 Guidetti, D., Murgia, M., Govoni, F., et al. 2008, *A&A*, **483**, 699  
 Harari, D., Mollerach, S., Roulet, E., & Sánchez, F. 2002, *JHEP*, **03**, 045  
 Hardcastle, M. J. 2013, *MNRAS*, **433**, 3364  
 Hitomi Collaboration, Aharonian, F., Akamatsu, H., et al. 2018, *PASJ*, **70**, 13  
 Hunter, J. D. 2007, *CSE*, **9**, 90  
 Irastorza, I. G., Avignone, F. T., Caspi, S., et al. 2011, *JCAP*, **2011**, 013  
 Irastorza, I. G., & Redondo, J. 2018, *PtPNP*, **102**, 89  
 Kachelriess, M., & Tjemsland, J. 2022, *JCAP*, **2022**, 025  
 Kalberla, P. M. W., Burton, W. B., Hartmann, D., et al. 2005, *A&A*, **440**, 775  
 Kale, R., & Parekh, V. 2016, *MNRAS*, **459**, 2940  
 Kim, J. E., & Carosi, G. 2010, *RvMP*, **82**, 557  
 Kuchar, P., & Enßlin, T. A. 2011, *A&A*, **529**, A13  
 Lam, S. K., Pitrou, A., & Seibert, S. 2015, Proc. of the Second Workshop on the LLVM Compiler Infrastructure in HPC, LLVM '15 (New York: Association for Computing Machinery),  
 Libanov, M., & Troitsky, S. 2020, *PhLB*, **802**, 135252

- Marsh, D. J. E. 2016, *PhR*, **643**, 1
- Marsh, M. D., Russell, H. R., Fabian, A. C., et al. 2017, *JCAP*, **12**, 036
- Marsh, M. C. D., Matthews, J. H., Reynolds, C., & Carena, P. 2022, *PhRvD*, **105**, 016013
- Matthews, J. H. 2022, alpro: Axion-Like PROpagation, v1.0, Zenodo, doi:10.5281/zenodo.6079445
- Mckinney, W. 2010, in Proc. of the 9th Python in Science Conf., ed. S. van der Walt & J. Millman (Austin, TX: SciPy), 56
- McNamara, A. L., Kuncic, Z., & Wu, K. 2009, *MNRAS*, **395**, 1507
- Meyer, M., Davies, J., & Kuhlmann, J. 2021, gammaALPs: Conversion probability between photons and axions/axionlike particles, Astrophysics Source Code Library, ascl:2109.001
- Meyer, M., Montanino, D., & Conrad, J. 2014, *JCAP*, **2014**, 003
- Mirizzi, A., Redondo, J., & Sigl, G. 2009, *JCAP*, **08**, 001
- Mukherjee, S., Khatri, R., & Wandelt, B. D. 2019, *JCAP*, **2019**, 031
- Mukherjee, S., Spergel, D. N., Khatri, R., & Wandelt, B. D. 2020, *JCAP*, **2020**, 032
- Murgia, M., Govoni, F., Feretti, L., et al. 2004, *A&A*, **424**, 429
- Nagai, H., Onishi, K., Kawakatu, N., et al. 2019, *ApJ*, **883**, 193
- Nandra, K., Barret, D., Barcons, X., et al. 2013, arXiv:1306.2307
- Pandas Development Team 2020, pandas-dev/pandas: Pandas, Zenodo, doi:10.5281/zenodo.3509134
- Payez, A., Evoli, C., Fischer, T., et al. 2015, *JCAP*, **2015**, 006
- Peccei, R. D., & Quinn, H. R. 1977, *ApJ*, **38**, 1440
- Perrone, L. M., & Latter, H. 2021, arXiv:2110.14696
- Pfrommer, C., & Enßlin, T. A. 2004, *MNRAS*, **352**, 76
- Planck Collaboration, Ade, P. A. R., Aghanim, N., et al. 2013, *A&A*, **550**, A131
- Preskill, J., Wise, M. B., & Wilczek, F. 1983, *PhLB*, **120**, 127
- Raffelt, G. G. 1996, Stars as Laboratories for Fundamental Physics : the Astrophysics of Neutrinos, Axions, and other Weakly Interacting Particles (Chicago, IL: Univ. Chicago Press)
- Raffelt, G. G. 2008, Axions, **741**, 51
- Raffelt, G., & Stodolsky, L. 1988, *PhRvD*, **37**, 1237
- Reynolds, C. S., Marsh, M. C. D., Russell, H. R., et al. 2020, *ApJ*, **890**, 59
- Reynolds, C. S., Smith, R. N., Fabian, A. C., et al. 2021, *MNRAS*, **507**, 5613
- Ringwald, A. 2012, *PDU*, **1**, 116
- Russell, H. R., Sanders, J. S., & Fabian, A. C. 2008, *MNRAS*, **390**, 1207
- Sanders, J. S., & Fabian, A. C. 2007, *MNRAS*, **381**, 1381
- Sanders, J. S., Fabian, A. C., & Dunn, R. J. H. 2005, *MNRAS*, **360**, 133
- Schallmoser, S., Krippendorf, S., Chadha-Day, F., & Weller, J. 2021, arXiv:2108.04827
- Schekochihin, A. A., & Cowley, S. C. 2006, *PhPI*, **13**, 056501
- Schekochihin, A. A., Cowley, S. C., Kulsrud, R. M., Hammett, G. W., & Sharma, P. 2005, *ApJ*, **629**, 139
- Schekochihin, A. A., Cowley, S. C., Taylor, S. F., Maron, J. L., & McWilliams, J. C. 2004, *ApJ*, **612**, 276
- Schnittman, J. D., & Krolik, J. H. 2010, *ApJ*, **712**, 908
- Sisk-Reynés, J., Matthews, J. H., Reynolds, C. S., et al. 2022, *MNRAS*, **510**, 1264
- Svrcek, P., & Witten, E. 2006, *JHEP*, **2006**, 051
- Taylor, G. B., Gugliucci, N. E., Fabian, A. C., et al. 2006, *MNRAS*, **368**, 1500
- Tribble, P. C. 1991, *MNRAS*, **253**, 147
- Ursini, F., Matt, G., Bianchi, S., et al. 2022, *MNRAS*, **510**, 3674
- Vazza, F., Brüggén, M., Gheller, C., & Wang, P. 2014, *MNRAS*, **445**, 3706
- Vazza, F., Brunetti, G., Brüggén, M., & Bonafede, A. 2018, *MNRAS*, **474**, 1672
- Virtanen, P., Gommers, R., Oliphant, T. E., et al. 2020, *NatMe*, **17**, 261
- Vogt, C., & Enßlin, T. A. 2005, *A&A*, **434**, 67
- Walker, S. A., ZuHone, J., Fabian, A., & Sanders, J. 2018, *NatAs*, **2**, 292
- Weinberg, S. 1978, *ApJ*, **40**, 223
- Wilczek, F. 1978, *ApJ*, **40**, 279
- Wouters, D., & Brun, P. 2012, *PhRvD*, **86**, 043005
- Wouters, D., & Brun, P. 2013, *ApJ*, **772**, 44
- Xu, H., Li, H., Collins, D. C., Li, S., & Norman, M. L. 2009, *ApJ*, **698**, L14
- Zhuravleva, I., Churazov, E., Schekochihin, A. A., et al. 2014, *Natur*, **515**, 85